

Final Draft
of the original manuscript:

Imandoust, A.; Barrett, C.D.; Al-Samman, T.; Tschopp, M.A.; Essadiqi, E.;
Hort, N.; El Kadiri, H.:

**Unraveling Recrystallization Mechanisms Governing Texture
Development from Rare-Earth Element Additions to Magnesium**

In: Metallurgical and Materials Transactions A (2018) Springer

DOI: 10.1007/s11661-018-4520-8

Unraveling Recrystallization Mechanisms Governing Texture Development from Rare-Earth Element Additions to Magnesium

A. Imandoust¹ and C. D. Barrett^{2,3}, T. Al-Samman⁴, M. A.
Tschopp⁵, E. Essadiqi⁶, N. Hort⁷, H. El Kadiri^{2,3}

¹Department of Mechanical Engineering,
Auburn University, Auburn, AL, USA

²Department of Mechanical Engineering,
Mississippi State University, Mississippi, MS, USA

³Center for Advanced Vehicular Systems,
Mississippi State University, Mississippi, MS, USA

⁴Institute of Physical Metallurgy and Metal Physics,
RWTH Aachen University, Aachen, Germany

⁵Army Research Laboratory, Aberdeen Proving Ground,
Aberdeen, MD, USA

⁶Aerospace Engineering School, Rabat, Université Internationale
de Rabat, UIR, Technopolis Shore Bypass, Rabat-Salé, Morocco

⁷Magnesium Innovation Centre, Helmholtz-Zentrum Geesthacht,
Max-Planck-Strasse 1, 21502, Geesthacht, Germany

Abstract

The origin of texture components often associated with rare-earth element (REE) additions in wrought magnesium alloys is a long-standing problem in magnesium technology. While their influence on the texture is unquestionable, it is not yet clear why certain texture components, such as $\langle 11\bar{2}1 \rangle \parallel$ extrusion direction; are favored over other components typically observed in traditional magnesium alloys. The objective of this research is to identify the mechanisms accountable for these RE textures during early stages of recrystallization. Electron backscattered diffraction and transmission electron microscopy analyses reveal that REEs in zinc-containing magnesium alloys corroborate discontinuous dynamic recrystallization. REEs promote isotropic growth for all nuclei generated through the bulging mechanism. During nucleation, the effect of REEs on orientation selection was explained by the diversified activity of both $\langle 10\bar{1}0 \rangle$ and $[0001]$ Taylor axes in the same grain with a marked preference for $[0001]$ rotations to occur first. During nuclei growth, no growth preference was observed when sufficient REEs are added in the zinc-containing magnesium alloys, instead isotropic nuclei growth across all grain orientations occurs. This phenomenon is attributed to REEs segregating to grain boundaries (GBs), in agreement with prior computational and theoretical results (Barrett et al., *Scripta Mater* 146:46–50, 2018) that show a more isotropic GB energy and mobility after segregation.

1 Introduction

The propensity for magnesium (Mg) to develop sharp textures during thermomechanical processing (TMP) has plagued its future as an ideal lightweight material in the automotive, aerospace, and defense applications. In a similar manner to single crystals, sharp textures respond to mechanical loads with strong anisotropy and asymmetry [1,2]. This can be problematic in application. For example, a typical rolled sheet cannot withstand large strains along arbitrary directions prior to fracture, a severe problem for forming of Mg alloys. Moreover, a thin-walled hollow tubes made from Mg alloys are observed to shatter into pieces prior to absorbing impact under crash conditions [3-10].

The ease of basal slip and the dislocation recovery mechanisms operating in Mg alloys have been long understood to promote sharp textures. Basal slip causes the basal poles to align themselves with the loading direction,[1,2] whereas dynamic recovery confines these planes to rotate, only around the $\langle c \rangle$ -axis within subgrains formed by prismatic dislocations, and the prismatic axes within subgrains constructed by basal and pyramidal dislocations [11,12]. Those types of rotations occur because [0001] is the Taylor axis for prismatic slip, while $\langle 10\bar{1}0 \rangle$ is the common one to both basal and pyramidal $\langle c+a \rangle$ slips [11,13-15]. Weak textures could have well developed if rotations could have been effected around an axis that deviates the $\langle c \rangle$ -axis from the main loading direction. However, there is no active slip mode with such a desirable Taylor axis.

Dynamic recrystallization (DRX) has been observed to occur either continuously (CDRX) or discontinuously (DDRX) depending on the temperature, strain, and strain rate. These external factors directly affect dislocation generation and multiplication at mantle regions, while microstructure and defects such as grain boundaries (GBs), solutes, and particles could either promote or limit the driving force underscored in dislocation recovery [16-22]. Regardless of the predominant DRX mechanism in the processing condition, the sharp deformation texture would be either untouched or further sharpened in traditional Mg alloys [2]. The most successful approach to overcome this shortage has recently been alloying with rare-earth elements (REEs) including cerium (Ce), gadolinium (Gd), neodymium (Nd), lanthanum (La), and yttrium (Y) all caused noticeable texture modifications, resulting in a reduction in the strength of the basal texture [15,23-25].

Not limited to texture weakening, REE additions were suggested to boost ductility by virtue of softening pyramidal $\langle c+a \rangle$ slip. Sandlöbes et al. [26,27] reported that additions of Y could bolster $\langle c+a \rangle$ dislocation activity because Y decreases the energy of the I_1 stacking fault (ISF_1), which acts as a nucleation site for $\langle c+a \rangle$ dislocations [28,29]. Ce and Nd additions were observed to cause similar non-basal slip enhancement by activating pyramidal $\langle a \rangle$ slip and by decreasing the critical resolved shear stress CRSS ratios between various active slip

modes [15,30,31]. Despite the ductility improvements associated with REEs in Mg, the required temperatures for acceptable formability of inner door panels still remain above 150 °C temperature, and one reason for this appears to be the fact that the texture after processing (although modified) is still sharp [23,32].

These limitations have provoked interest in the mechanisms through which REEs modify textures, motivating research that will lead to identifying a rational design strategy that can harness the beneficial effects of REE to reach the required properties and performance of these alloys. Hantzsche et al. [33] and several other authors such as Hadorn et al. [15] showed that a compositional threshold exists for each REE whereupon texture intensity drops drastically. Several researchers reported that the essential texture weakening takes place upon DRX [23-25,33,34]. Bohlen et al. [23] and Barnett et al. [35] confirmed that a recrystallized portion of the microstructure under extrusion has always a $\langle 11\bar{2}1 \rangle \parallel$ ED (extrusion direction) component, characteristic of REEs, and hence referred to as "RE texture" [24,25]. A $\langle 10\bar{1}0 \rangle \parallel$ ED fiber with lower intensity was also reported to emerge with the RE texture. Furthermore, the RE texture is able to survive subsequent nuclei growth, which correlates with further texture randomization phenomena [23,25,33,36-38]. The origin of the RE texture is a metallurgical conundrum, added atop of the mechanisms underlying the effect of REEs on texture weakening.

Research experience with the legacy of cubic materials triggered a few authors to propose the so-called *particle stimulated nucleation* (PSN) as responsible for the rise of new orientations which do not occur in classical Mg alloys,[39,40] thereby, advocating for discontinuous DRX (DDRX). However, Al-Samman and Li [41] showed that RE texture and texture weakening can occur, even in cases where the fraction of RE-containing precipitates remains too dismal to bring about a macroscopic effect. Robson et al. [42] confirmed that grains that recrystallized close to GBs attained larger sizes and survived longer than those recrystallized by a PSN effect.

As the PSN mechanism began to prove less than ideal, a few authors such as Hadorn et al. [43] suggested that REEs in solid solution could actually alter the *deformation mechanisms* in a way that disrupts how geometrically necessary dislocation (GND) structures develop in the material. On a related note, Stanford[24] indicated that RE effect greatly depends upon the way solute atoms interact with both dislocations and GBs. A GB with segregated RE solutes becomes sluggish,[36,43-45] and hence, more resistant to migration and/or bulging, which are essential phenomena for continuous DRX to operate [36]. Nie et al. [46] showed in fact a periodic segregation pattern in twin boundaries (TBs), while Hadorn et al. [44] confirmed that segregation proceeds without a truly describable pattern in high angle GBs. Therefore, CDRX and DDRX might be concomitantly

active over the course of any TMP, making nucleation and growth of DRX nuclei with the RE texture difficult to examine under the microscope.

Stanford and Barnett[25] captured RE-textured grains forming within *shear bands* in a Mg-RE alloy, while the rest of recrystallized grains predominantly adopt a $\langle 11\bar{2}0 \rangle$ fiber. Sandlöbes et al. [27] corroborated this proposal and further observed that REEs promote a more uniform distribution of shear bands. However, results from several authors[15,23,30,43,47] showed the omnipresence of RE texture without any prior formation of shear bands, thus removing the shear band hypothesis from the list of required root-cause mechanisms. Stability of RE-oriented nuclei is another aspect to this puzzle, where there might be a handful of randomly oriented nuclei that do not get the chance for further growth [3]. Such nucleation sites would remain undiscovered due to the rather large progress of DRX after processing.

One could also envisage that REEs do not promote nucleation of RE-textured embryos per se, but only promote their stability during the growth stages. Thus, the role of nuclei growth in the grain orientation selection/elimination process must be clarified. While traditional Mg alloys tend to sharpen their texture during static annealing,[3,48] RE-containing Mg alloys do exactly the opposite [33]. Accordingly, one can hypothesize that RE addition manipulates growth preferences with a specific bias [41].

Recent analyses by the present authors of the misorientation relationships that occur between recrystallized grains and their parents in traditional Mg alloys (AM30) demonstrated the key role that GB energy and mobility play in texture formation and stabilization during nucleation and growth of recrystallized grains, respectively. Cusps in GB energy around a given Taylor axis acts as a trap for rotations of subgrain, prompting them to settle at singular boundaries, usually TBs, and as such, only a few orientations became favored during the nucleation process. Moreover, some of these boundaries have extremely high mobility, seeing their grains grow abnormally and prevail in the final texture. In this paper, we hypothesize that these mechanisms, which explain sharp texturing in classical Mg alloys, are altered by REEs in a fashion that would lead to the RE texture and ensuing texture randomization. This hypothesis is supported by the universal agreement that REEs tend to segregate at GBs [42]. Strong GB drag effects have been observed in ternary alloys containing both Ca and Zn, which suggests important co-segregation effects beyond solute segregation of the individual species [49]. We attempt to identify some of the key mechanisms that govern the effect of REEs on the behavior of GBs during nucleation and nuclei growth.

We examine four REE-containing alloys with different DRX resistance, and vary the processing conditions to track the changes in microstructure and texture evolutions from the nucleation stage to the point where the grain growth stage is nearly completed. Exploiting predesigned processing parameters enables us to

identify the most important nucleation sites, and examine the influence of static and DRX on the growth of nuclei/grains with new orientations.

2 Experimental Procedure

2.1 Alloy Compositions

We tested four alloys containing Al, Mn, and Y but with varying concentrations of Zn and Mischmetal (MM, see Table 1), and applied two extrusion speeds to all of them. The purpose of adding Al, Mn, and Zn was to understand the effect of REEs on RE-texture formation within complex alloy compositions that have recently been developed by alloy designers. In fact, Mn additions are usually added to getter Fe from solid solution, which would be otherwise deleterious to the corrosion resistance. The Al content was higher than most Mg-RE alloys (>0.2 pct), but as we will see, it did not hamper formation of RE-texture components.

Zn content was high in two alloys (1.2 wt pct for Alloys A and B) and low for the other two (0.4 wt pct, Alloys C and D). One of the Zn-rich alloys (Alloy B) was enriched in MM, while the other one was left without, and the same was applied for the two other alloys with low Zn content. Y was added to all the four alloys with a concentration substantially above the threshold for texture weakening observed in binary Mg-Y alloys. However, one should bear in mind that presence of Zn and Al may change the threshold limit as Y tends to segregate into the Mg-Zn-Y precipitates and RE-containing aluminides [41,50]. Nevertheless, the nominal content of Y was high enough to enable RE-texture formation even in alloys with highest concentrations of Zn and Al, and no MM.

MM has slow bulk diffusion in Mg, so when it exists in high concentrations (e.g., Alloy B), particularly when accompanied by Zn, recrystallization kinetics are expected to be relatively slower. In fact, co-segregation of Zn and MM into the GBs is believed to retard recrystallization kinetics [49]. As such, their effect will be important during nuclei growth when the kinetics of recrystallization are counterbalanced by a high extrusion speed, promoting the density of nucleation sites through larger area reduction/plastic strain. In contrast, at low extrusion speed, where recrystallization is supposed to be slow, the absence of MM (Alloys A and C) makes it suitable to observe the effect of Y on the development of RE texture during grain nucleation. In general, the slow recrystallization kinetics at low extrusion speed are expected to allow tracing nucleation of grains with an RE/random texture type orientation at early stages for all alloys as they all contain Y. Similarly, the fast kinetics are expected to allow appreciating how varying concentrations of REEs, with or without Zn, affect the overall texture strength

Table 1: Chemical Composition of Alloys in wt pct Measured by ICP-AES Method

Alloys	Composition (Wt Pct)				
	Zn	Al	Mn	Y	MM
A	1.20	0.53	0.27	1.70	0.02
B	1.10	0.49	0.30	2.20	0.41
C	0.40	0.57	0.29	2.05	-
D	0.41	0.58	0.29	2.04	0.30

The balance metal is Mg. MM composition: 55.90 Ce-30.50 La-6.80 Pd-5.20 Nd-1.60 others (wt pct).

and RE-texture development during DRX and nuclei/grain growth. The chemical composition of the alloys are listed in Table 1.

2.2 Experiments

The alloy billets, in cast condition, were solution annealed at 450 °C for 10 hours under flowing argon gas atmosphere followed by immediate water quenching. After annealing, the chemical composition was analyzed using atomic emission spectroscopy (ICP-AES) method. Solution-treated alloys were machined to cylindrical specimens ~ 32 mm (1.25 in.) in diameter and ~ 25 mm (1 in.) and were subject to indirect extrusion at ram speeds of 10 and 40 mm/min with an area reduction ratio of 6 at 450 °C followed by air cooling. It should be noted that conducting extrusion increased the actual temperature by 5 °C to 7 °C, which is believed to have a consistently minor effect in the texture and microstructure evolutions during DRX. It is worth noting that static recrystallization, though minor, could take place during air cooling of the extrudates. In order to observe the individual effect of static recrystallization and further nuclei/grain growth, post annealing was conducted for 20 and 180 minutes at 450 °C on select samples. Samples were cut along the radial and transverse directions to examine the microstructural and texture evolutions on planes normal to ED and normal to extrusion radial direction (ERD). The ERD is a radial direction of the cylinder that is normal to ED.

The different samples were then characterized using several different techniques. Samples were extracted from the center of the extrudates in the steady-state region, and were grounded by standard metallographic techniques and polished using 0.06 μm colloidal silica (Struers OPS) for 10 minutes. In preparation for electron backscattered diffraction (EBSD), electro-polishing was carried out on polished samples in chilled Struers C1 solution at 25 V for 120 seconds. Sam-

ples were sonicated for 20 minutes after preparation in absolute ethanol to remove artifacts from the surface. Texture measurements were conducted on transverse cross-sectional (plane normal to ERD) and radial cross-sectional (plane normal to ED) planes using EBSD and X-ray diffraction (XRD), respectively. EBSD analyses were performed using a field emission scanning electron microscope (SEM) at the operating voltage of 20 kV.

In order to acquire statistically reliable data, several EBSD scans were performed on the selected samples, and the best representative results are used in the present paper. XRD macro-texture measurements were conducted by measuring six incomplete experimental pole figures from $\alpha = 5$ to 80 deg using Cu $K\alpha$ radiation at 40 kV and 30 mA with a Rigaku SmartLab facility. The experimental pole figures ($\{0002\}$, $\{10\bar{1}0\}$; $\{10\bar{1}0\}$; $\{1012\}$; $\{1013\}$; $\{11\bar{2}0\}$) were used to calculate the orientation distribution function using MTEX toolbox in MATLAB [51]. The validity of macro-texture results was confirmed by selecting four samples from the center of each extrudate. Transmission electron microscopy (TEM) disks with 3 mm in diameter were punched from foils grounded to the thickness of 200 μm followed by ion milling at 3.5 kV until perforation. TEM imaging and STEM EDX analysis were conducted by a JEOL 2100 TEM operating at 200 kV.

3 Results and Discussion

The outcomes of this study are organized in the following manner. The experimental results are separated into the texture and microstructure evolutions during low- and high-speed extrusions (Section III–A). Section III–B explores DRX nucleation sites and the role of active recrystallization mechanisms exploiting low-speed extrusions in the early stages of recrystallization. Afterwards, the results of fast extrusion along with post annealing not only did display the significance of the grain growth on texture evolutions, but also unraveled some discernable distinctions in the texture patterns of the dynamically and statically recrystallized samples.

3.1 Influence of Chemical Composition and Extrusion Condition

In order to analyze the effect of extrusion condition and chemical composition on texture modification of RE, a series of extrusions at 10 and 40 mm/min and 450 °C were conducted. Faster recrystallization kinetics during high-speed extrusion pertain to a higher nucleation rate of DRX grains, which is granted by the high level of the strain energy delivered and stored in the matrix.

3.1.1 Texture evolution

3.1.1.1 Low-speed extrusions Figures 1(a) through (d) show recalculated XRD inverse pole figures of the four slowly extruded alloys. Recalculated inverse pole figures reveal a quite strong $\langle 10\bar{1}0 \rangle \parallel$ ED fiber texture along with a relatively weak RE texture. This RE texture has been identified to lie very closely to $\langle 22\bar{4}3 \rangle \parallel$ ED component. For traditional Mg alloys, $\langle 10\bar{1}0 \rangle$ fiber has been shown to correlate with the parent grains and a portion of the recrystallized grains [52]. For the parent grains, it results from extensive basal, pyramidal $\langle c+a \rangle$ and prismatic slip modes, which, having the $\langle 10\bar{1}0 \rangle$ and $[0001]$ as Taylor axes, respectively, align the basal planes with ED. Our texture and micro-texture analyses indicate that this must be also the case for the present alloys.

Due to small area reduction ratio (i.e., 1:6) and thus, probably a lack of sufficient stored deformation energy, approximately over 85 pct area fraction of the microstructures in Figures 1(a) through (d) are composed of deformed grains. Hence, the texture intensities remain noticeably high. However, these high texture intensities did not prohibit formation of strong RE-texture component [33]. This must be due to the relatively pronounced presence of Y, which despite the presence of Zn, Al, and Mn and their ability to reduce its solid solution content by precipitation (see Section 3.2.2.3), was added in sufficient quantities to prompt nucleation of grains with orientations characterizing the effect of REEs (Figures 1(a) and (c)).

However, relying only on the content of REEs to expect texture weakening entails that Alloys D and B, having the highest contents of MM should have the weakest texture of them all. In reality, Alloy C has the lowest maximum texture intensity value among the slowly extruded billets. This apparent contention is explained by the difference in the rate of recrystallization, which is relatively faster in Alloy C with no MM. As previously indicated, the kinetics of recrystallization is dependent upon the combined amount of Zn, Y, and MM content of the alloys which would tend to slow down recrystallization. In fact, a high combined content of these elements could result in an increased mutual segregation and/or diffusion in dislocation core, which would hamper GB and/or dislocation mobility [49]. Therefore, it is no wonder why Alloy C, having the lowest net content of Zn, Y, and MM, developed the lowest texture intensities. Actually, according to this interpretation, the kinetics are expected to be faster in the following order: Alloy C \geq Alloy D \gg Alloy A $>$ Alloy B, which is fully consistent with our observations (Figure 2).

However, as the development of RE texture hinges on mutually fast recrystallization kinetics and higher REE concentrations, Alloys A and C showed higher intensities of RE texture than Alloys B and D (Figure 1). Alloys A and C in fact had sufficient fraction of DRX grains for the RE texture to emerge in the texture

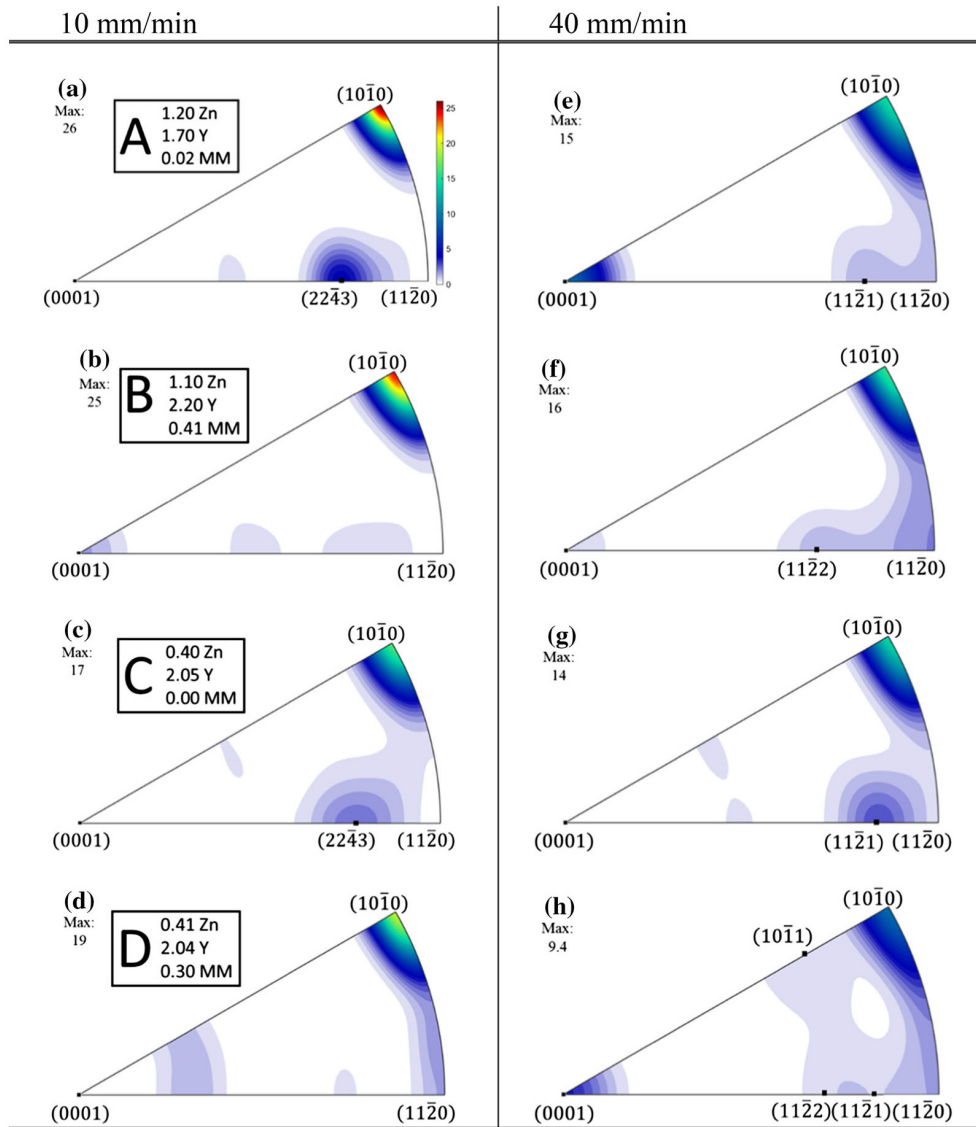


Figure 1: Recalculated inverse pole figures (IPFs) after 10 and 40 mm/min – 450 °C extrusion (with 1:6 area reduction ratio) of (a, e) Alloy A with 1.2 pct zinc and 0.02 pct Mischmetal; (b, f) Alloy B with 1.1 pct zinc and 0.41 pct Mischmetal; (c, g) Alloy C with and 0.4 pct zinc and no Mischmetal, and (d, h) Alloy D with 0.41 pct zinc and 0.31 pct Mischmetal. All alloys contain about 2 pct of yttrium. The accuracy of texture measurements was ± 0.2 . IPFs refer to extrusion direction. The concentration of key elements are also noted on the IPFs in wt pct.

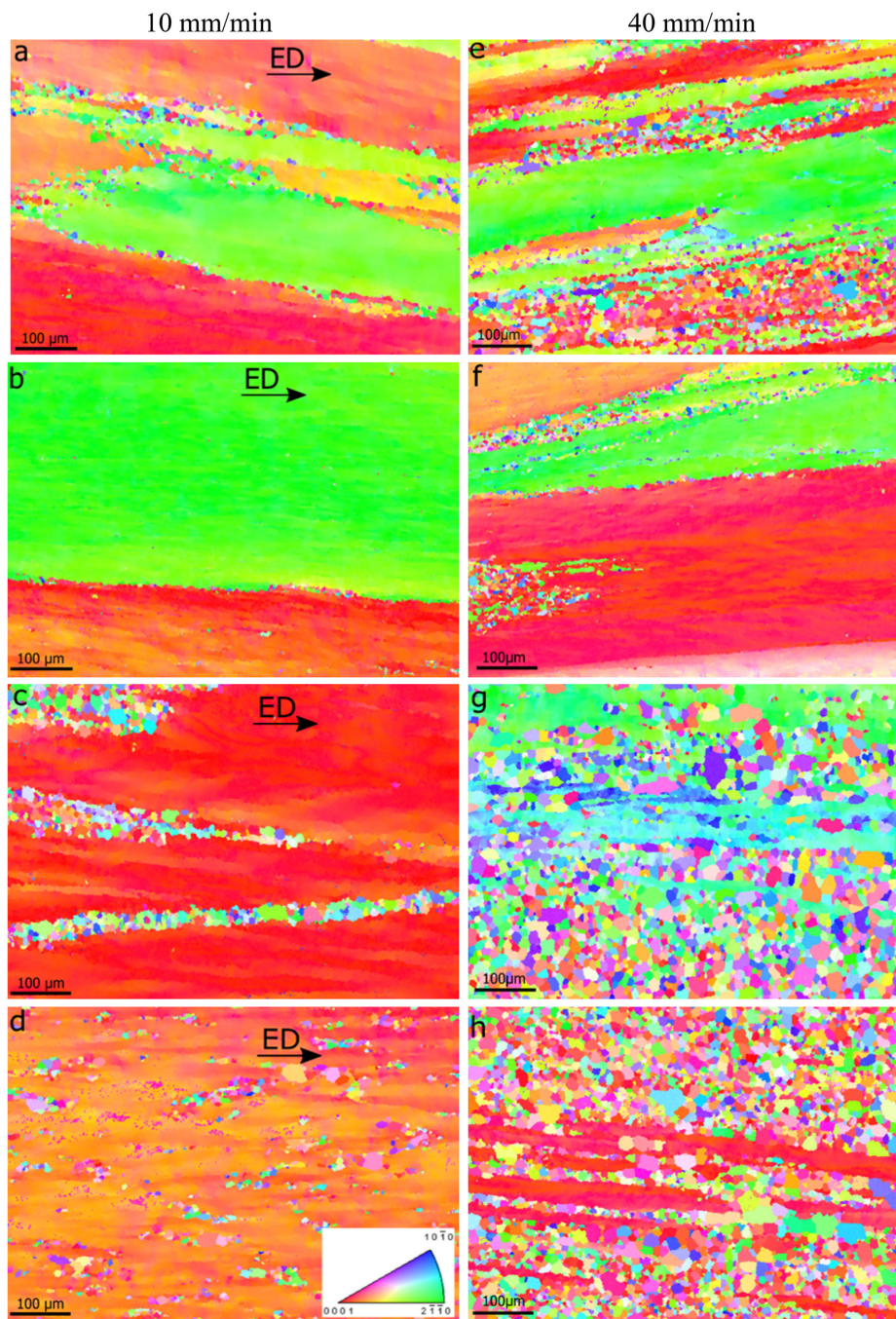


Figure 2: Inverse pole figure maps of (a, e) Alloy A with 1.2 pct zinc and 0.02 pct Mischmetal, (b, f) Alloy B with 1.1 pct zinc and 0.41 pct Mischmetal, (c, g) Alloy C with 0.40 pct zinc and no Mischmetal, and (d, h) Alloy D with 0.41 pct zinc and 0.30 pct Mischmetal after 10 and 40 mm/min – 450 °C extrusion with 1:6 area reduction ratio. The concentration of key elements are in wt pct.

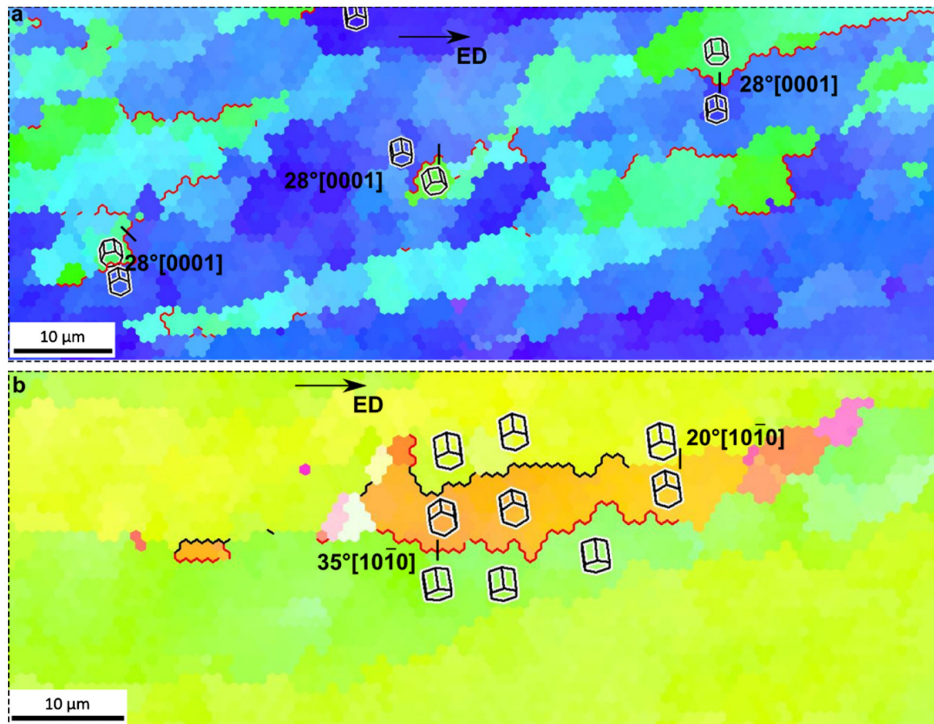


Figure 3: Electron backscattered diffraction analyses revealing dynamic recovery taking place in Alloy B extruded at 450 °C with 10 mm/min ram speed. (a) An inverse pole figure ED map showing continuous dynamic recrystallization by 28 deg rotation around [0001] axis. (b) An inverse pole figure ND map showing continuous dynamic recrystallization by rotations around $\langle 10\bar{1}0 \rangle$.

plots. Y and MM ought to be high enough to produce typical RE effect, while net Zn, Y and MM concentration should be sufficiently low to allow for reasonable amount of recrystallization to occur. That is, while the texture component became more diversified as MM concentrations increased, RE-texture evolution was substantially delayed so much so that it was hardly any visible in Alloy B.

From a statistical point of view, the intensity of RE texture depends on the density of available nucleation sites and the stability of their nucleated grains during the nuclei growth stages. For instance, EBSD analyses indicate that Alloy A (with less MM content) has relatively thinner bands of deformed grains than Alloy B, and hence more GB area and a higher probability for the RE orientations to nucleate are noticed (Figures 2(a) and (b)). It is worth mentioning that continuous rotation of cell-structures within the bands of deformed grains during extrusion eliminated the effects of initial grain size on their thickness (Figure 3). As mentioned, DRX kinetics were very sluggish in Alloy B due to the higher

concentrations of MM that obstruct GB motion [36]. Hence, in stark agreement with the results of recalculated IPFs shown in Figure 1, Alloy B has less potential for developing RE texture than Alloy A. Furthermore, Alloys C and D with slightly higher volume fraction of DRX grains than Alloys A and B, as illustrated by Figures 2(a) through (d), exhibit smaller maximum texture intensities (Figure 1). Comparing the IPFs of Alloys C and D in Figure 1 proves that the intensity of RE-texture component is directly connected to the DRX kinetics. Having undergone slower DRX kinetics due to the greater net amount of MM, Alloy D develops reduced RE-texture intensities than Alloy C (no MM additions). Finally, Alloy D displays a weaker texture compared to all other alloys, which had either a slower recrystallization rate (Alloy B) or a lower fraction of MM content (Alloy C). Thus, Y proves less effective than MM in texture modification.

3.1.1.2 High-speed extrusions The highly stored energy level associated with the high-speed extrusion allowed substantial texture weakening, as intensities were approximately 10 m.r.d. (multiple of a random distribution) less than those retrieved from low-speed extrusion (Figure 1). IPF mapping shows that Alloys C and D have developed a higher fraction of DRX grains and a wider range of texture components than Alloys A and B (Figures 2(e) through (h)). However, RE texture (e.g., $\langle 11\bar{2}1 \rangle \parallel ED$) was pervasive in all the four alloys. Alloy D exhibited the most versatile texture components owing to the added presence of MM. In contrast, Alloy A not only recrystallized slower, it did not benefit from MM. However, it still shows RE texture atop of a stronger $[0001] \parallel ED$ component. This phenomenon underscores that the all alloys tend to develop RE texture during the nucleation stage, but it is just a problem of the kinetics for this texture to manifest itself in the IPFs.

As pointed out, in addition to a pervasive $\langle 11\bar{2}1 \rangle \parallel ED$ texture component for all alloys, there is a fairly high fraction of grains having the basal pole parallel to ED, i.e., $[0001] \parallel ED$ (Figures 2(e) through (h)). These grains have been detected in IPF maps, revealing that the misorientation angle and axis across the GB are approximately 90 ± 2 deg and $13\bar{2}714\bar{1}$; respectively. This misorientation axis is actually very close to $\langle 1\bar{2}10 \rangle$. There are two very low energy GBs that fall close to this misorientation relationship. First is the coherent $\{1012\}$ TB with about 87 deg misorientation angle, and the second is the basal-prismatic (BP) asymmetric tilt GB with 90 deg misorientation. Barrett and El Kadiri[53] demonstrated that the BP boundary develops the lowest excessive potential energy among all asymmetric tilt boundaries observed in the literature. In addition, it systematically facets with the $\{1012\}$ TB making it easy to form two-dimensional embryos. The low energy of this type of boundary may be a driving force for DDRX/parent in-

terface may be the driving force for nucleation and migration of such a boundary, leading to a new texture component in the microstructure.

3.1.2 Microstructural observations

Figure 2 shows typical microstructures obtained by slow and fast extrusion. One can observe that extrusion speed changes the DRX volume fraction significantly, which insinuates the dominance of DRX over static recrystallization during air cooling of the as-extruded billets. The grains in pancake-like morphology lying parallel to the ED correspond to parent grains. Their orientations are majorly clustered near the $\langle 10\bar{1}0 \rangle \parallel$ ED fiber, accounting for the sharp texture intensities in the calculated inverse pole figures in Figure 1. Both shape and orientation of grains develop in a similar fashion as in traditional Mg alloys, prompting GBs with a predominant tilt character.

Alloy B shows comparatively a dearth of recrystallized grains (Figures 2(b) and (f)) but very large parent grains. Next, recrystallized grains in fine lines are detectable in Alloy A as they nucleate on GBs between parent grains. Alloy D exhibits a higher fraction of recrystallized grains than Alloy A, but they seem to spread more homogeneously in the matrix, whereas GBs of parent grains remain harder to define. In Alloy C, uninterrupted necklaces of recrystallized grains decorate most GBs in relatively thick lines. These microstructural observations substantiate the order of recrystallization kinetics between the four alloys described in the previous section.

3.2 Contribution of Recrystallization Mechanisms

One approach to elucidate the mechanisms of DRX is to generate partially recrystallized microstructures in which it is possible to find recrystallized and parent grains together, allowing details of the misorientation relationships between the two to be examined. In this study, we were able to track the DRX behavior from the very early stages by performing low-speed and low area reduction ratio types of extrusions on Mg-RE alloys, having various levels of DRX resistance. As such, we are able to assess the relative contributions of concurrently active DRX mechanisms in the development of new texture components.

3.2.1 Continuous dynamic recrystallization, CDRX

The slow recrystallization kinetics in Alloy B, having the highest sum of Y, MM, and Zn concentrations among all other alloys, and low-speed extrusion enabled us to capture early stages of CDRX. The IPF maps of Figure 3 illustrate that CDRX occurs in Alloy B through formation of elongated grains with $\langle 10\bar{1}0 \rangle$ fiber texture

component (Figure 3(a)), which may result in a sharper fiber texture. Although some of the present authors found the CDRX mechanism to be responsible for texture modifications in high purity binary Mg-RE alloys,[54] this mechanism does not seem to be influential for the experimental alloys in this study. Actually, CDRX assisted the parent grains to rotate around their $\langle 10\bar{1}0 \rangle$ poles by rotation of sub-grains, and they contribute to the $\langle 10\bar{1}0 \rangle$ fiber texture component in the extruded condition, in good agreement with XRD recalculated inverse pole figures (Figure 1(b)). Rotation around [0001] occasionally took place (Figure 3(b)), revealing the formation of sub-grains from arrays of prismatic dislocations. This seems to be also in good agreement with the results by Hadorn et al. [43] who reported the predominance of either [0001] or $\langle 10\bar{1}0 \rangle$ Taylor axes but not both in any CDRX grain nucleation event. After the rotation of sub-grains inside the elongated grains, wide bands of deformed grains set the stage for other restoration mechanisms to begin.

3.2.2 Discontinuous dynamic recrystallization, DDRX

Throughout our microstructural investigations, we observed immense activity of bulging and nucleation of recrystallized grains at the GB protrusions, which is fully consistent with DDRX [55]. Therefore, we focus on this mechanism and its consequent effects on texture nucleation in detail.

3.2.2.1 Nucleation sites Figures 4 and 5 depict typical misorientation profiles and their corresponding axis/ angles. The IPF maps were taken from planes normal to ERD. The misorientation axes for all the calculated axes/angles correspond essentially to $\langle 10\bar{1}0 \rangle$ with slight deviations due to the relatively trivial activity of other slip modes [3]. The range of measured angles was ~ 70 to 80 deg for interfaces between bands with orientations close to $[0002] / \langle 11\bar{2}1 \rangle \parallel \text{ERD}$; ~ 41 to 52 deg for ones close to $\langle 11\bar{2}0 \rangle / \langle 11\bar{2}1 \rangle \parallel \text{ERD}$; ~ 51 to 60 deg for ones close to $\langle 11\bar{2}0 \rangle = \langle 11\bar{2}3 \rangle \parallel \text{ERD}$ and ~ 21 to 24 deg for ones close to $\langle 11\bar{2}1 \rangle = \langle 11\bar{2}3 \rangle \parallel \text{ERD}$. Assuming those interfaces to be perfectly aligned with the corresponding poles, the misorientation angles would be $2\Theta = 61.4$ deg for $[0002] / \langle 11\bar{2}1 \rangle$ interface, $2\Theta = 47.1$ deg for $\langle 11\bar{2}1 \rangle / \langle 11\bar{2}0 \rangle$; $2\Theta = 58.3$ deg for $\langle 11\bar{2}0 \rangle / \langle 11\bar{2}3 \rangle$; $2\Theta = 11.1$ deg for $\langle 11\bar{2}1 \rangle / \langle 11\bar{2}3 \rangle$. Differences between the calculated and measured angles are attributed to the misalignment between actual directions and presumed ones. It is worth noting that the frequent presence of these boundaries could be rationalized by their low energy, which makes them more favorable during dislocation recovery (see Figures 3 and 5).

Atomistic simulations have helped to explain some of the observed GBs within experimental samples. For example, Wang and Beyerlein[56] calculated angles for $\langle 10\bar{1}0 \rangle$ symmetric tilt GBs (STGB)s in Mg. Tilt angle, Θ , locate at 28.41

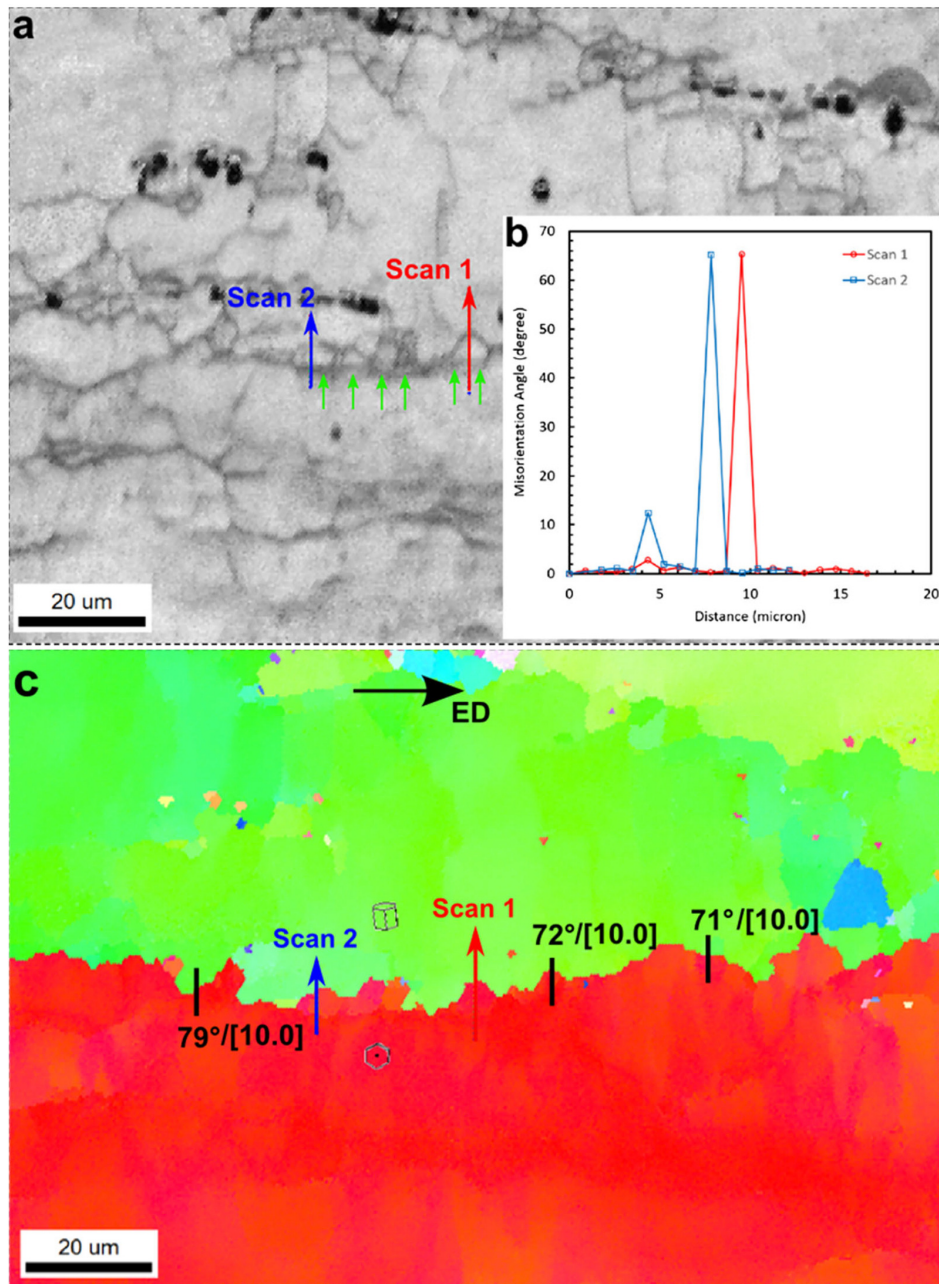


Figure 4: Electron backscattered analyses in terms of (a) an image quality map and (c) corresponding inverse pole figure maps revealing substantial bulging of a very stable 70 to 80 deg/ $\{<10\bar{1}0>\}$ boundary with minimum misorientation fluctuation along the interface. The image quality map reveals also the formation of low-angle boundaries at the backside of most grain boundary protrusions (indicated by green arrows). (b) The misorientation angle of these low-angle boundaries range from 2 to 10 deg indicating the occurrence of DDRX (Color figure online).

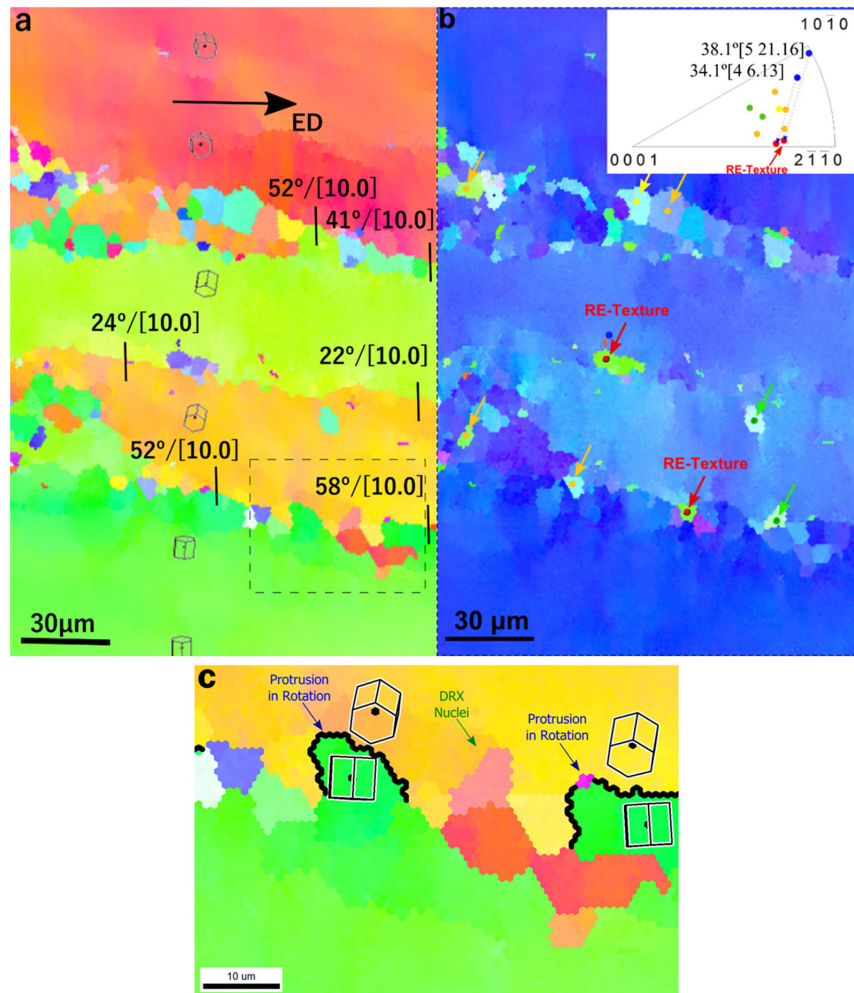


Figure 5: Inverse pole figure maps of Alloy A extruded at 450 °C with 10 mm/min ram speed revealing (a) high angle boundaries subject to recrystallization through the bulging mechanism. The ED-mapped IPF in (b) allowed discerning grains with orientations characteristic to the effect of rare earth including the RE texture (indicated with red arrows). The IPF map illustrates the rotation of two parent grains toward the RE-texture orientations as well as formation of several random orientations from the same parents. The IPF map in (c) reveals two protrusions still in intermediate stages of recrystallization as well as some protrusions that almost completed the recrystallization process by developing into a grain with random orientation, which were indicated by arrows in (b) (Color figure online).

deg, 39.06 deg, 58.36 deg, 72.88 deg for the observed energy cusps in the excess potential energies diagram for $\langle 10\bar{1}0 \rangle$ STGBs. In addition to STGBs, quite a few asymmetric tilt boundaries have been identified for HCP structures. Bruggeman et al. [57]. identified the potential symmetric and asymmetric tilt boundaries for rotations around $\langle 10\bar{1}0 \rangle$; $\langle 11\bar{2}0 \rangle$; [0001] axes based on the coincidence-site lattice (CSL) and near-CSL theory. According to this theory, in near-CSLs for $\langle 10\bar{1}0 \rangle$ tilt boundaries some asymmetric structural units would possess shorter periods than symmetric structural units, and hence, many of the $\langle 10\bar{1}0 \rangle$ tilt boundaries composed of short structural units are asymmetric. The potential near-CSL $\langle 10\bar{1}0 \rangle$ tilt boundaries identified by Bruggeman et al. [57] are as follows: $\Sigma 10$ with $2\Theta = 78.6_{0.5}^{+0.2}$; $\Sigma 11$ with $2\Theta = 62.8_{-0.1}^{+0.5}$; $\Sigma 11$ with $2\Theta = 35.2_{-1.1}^{+0.7}$; $\Sigma 14$ with $2\Theta = 44.4_{-0.2}^{+0.2}$ and $\Sigma 25$ with. Among the actual GBs captured in the microstructures, ones with 2Θ values of ~ 70 to 80 deg, ~ 51 to 60 deg, ~ 41 to 52 deg, and ~ 21 to 24 deg seem to fall very close to $\Sigma 10$ or $(\bar{2}114)$ STGB, $(\bar{2}116)$ STGB, $\Sigma 14$ and $\Sigma 25$ near-CSL boundaries, respectively. As mentioned above, the rotation axis was rather close to $\langle 10\bar{1}0 \rangle$. Actually, the close match between the theoretical and experimental axis/angles may suggest that the low energy of such GBs is the reason behind their abundance. As such, they are frequently observed in Mg and HCP microstructures, and they are the most active sites for nucleation of grains with new orientations including RE component.

3.2.2.2 Evidence of bulging The relatively slow recrystallization kinetics in Alloy A allowed revealing an important feature in the deformed portion of the microstructure. Throughout the sample, GBs between parent grains display significant serrations, which manifest as local protrusions of about $5 \mu\text{m}$ in diameter spreading along the entire interface length (Figures 4(a) and (c)). These GB protrusions correspond to bulging phenomena that have been traditionally associated with DDRX events [3]. Close examination of many locations in Figure 4 shows that the GB misorientation remains pretty much the same along the wavy interface, indicating that the boundary misorientation is relatively stable with respect to the action of plastic deformation (Figures 4(a) through (c)).

Traditionally, GBs act as an effective source of defects and host much of the sub-grain formation during recovery, so their associated misorientations tend to fluctuate. Figure 6 is a bright-field STEM image with EDAX mapping of Zn and Y in Alloy A taken at areas adjoining a GB. These chemical analyses reveal the segregation of Zn to the GBs. By co-segregating to GB free volume sites or substituting for Mg GB sites, Zn and Y co-segregation may lead to significant solute drag effects. [43,44,46] Zn in classical alloys such as AZ31 or AZ61, though added with concentrations as high as in Alloy A, does not segregate with as much intensities. Nie et al. [46] observed in fact a strong co-segregation potential of

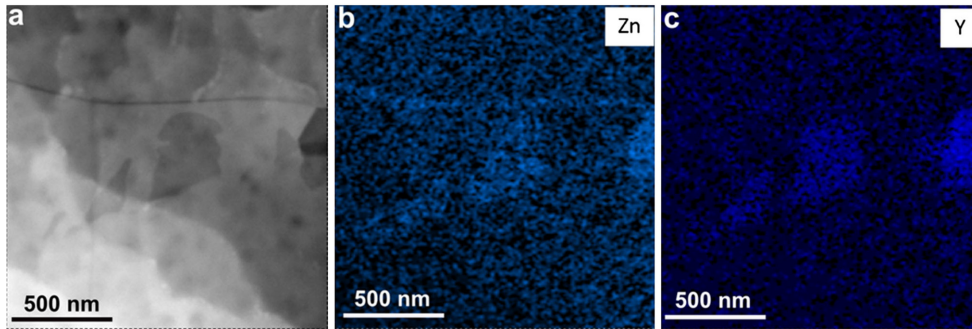


Figure 6: (a) A bright-field scanning transmission electron microscopy (STEM) image of a region taken near a grain boundary in Alloy A on which energy dispersive X-ray mapping of (b) zinc, (c) yttrium revealed substantial segregation of zinc into the boundary. Moreover, intermetallic particles seems to be rich with zinc and yttrium after extrusion at 450 °C and under 10 mm/min ram speed.

Gd and Zn in Mg, which is greater than if either Zn or Gd exist in the alloy. Similar co-segregation enhancements were observed when Ca was added atop of Zn [49,58]. This binding effect is attributed to the atomic size effects (small: Zn) and (large: Gd, Y) [59].

3.2.2.3 Bulging mechanism Bulging along GBs during high temperature recrystallization comprises two stages that are essential for describing the effect of REEs. The first stage corresponds to the mechanisms that drive migration of the GB, while the second stage relates to the inhomogeneity of this migration, giving rise to the observed protrusions.

During high temperature deformation, dislocation climb and cross-slip are common modes of recovery. It has been widely admitted that REEs of the likes of Y and MM, when added to Mg, tend to reduce the stacking fault energy on basal planes,[27] and hence, disrupt the ease of cross-slip and climb [20]. Inhibiting recovery processes sets the stage for recrystallization by a range of mechanisms including the GB migration mechanism known as strain-induced boundary migration, or SIBM [55].

TEM and STEM analyses revealed precipitates, which could contribute to the serrated structure of the interface (Figures 7(a) and (b)). Upon migration, GB may have advanced in the spaces between particles so its surface became bulged around precipitates. These fine particles had long periodic hexagonal structure Mg solid solution and cube $Mg_{24}Y_5$ [60]. STEM analyses also revealed particles that were rich in Y, Zn and Al (Figures 8(a) through (d)), suggesting they correspond to the eutectic b (FCC) phase which was identified in ternary and complex Mg-

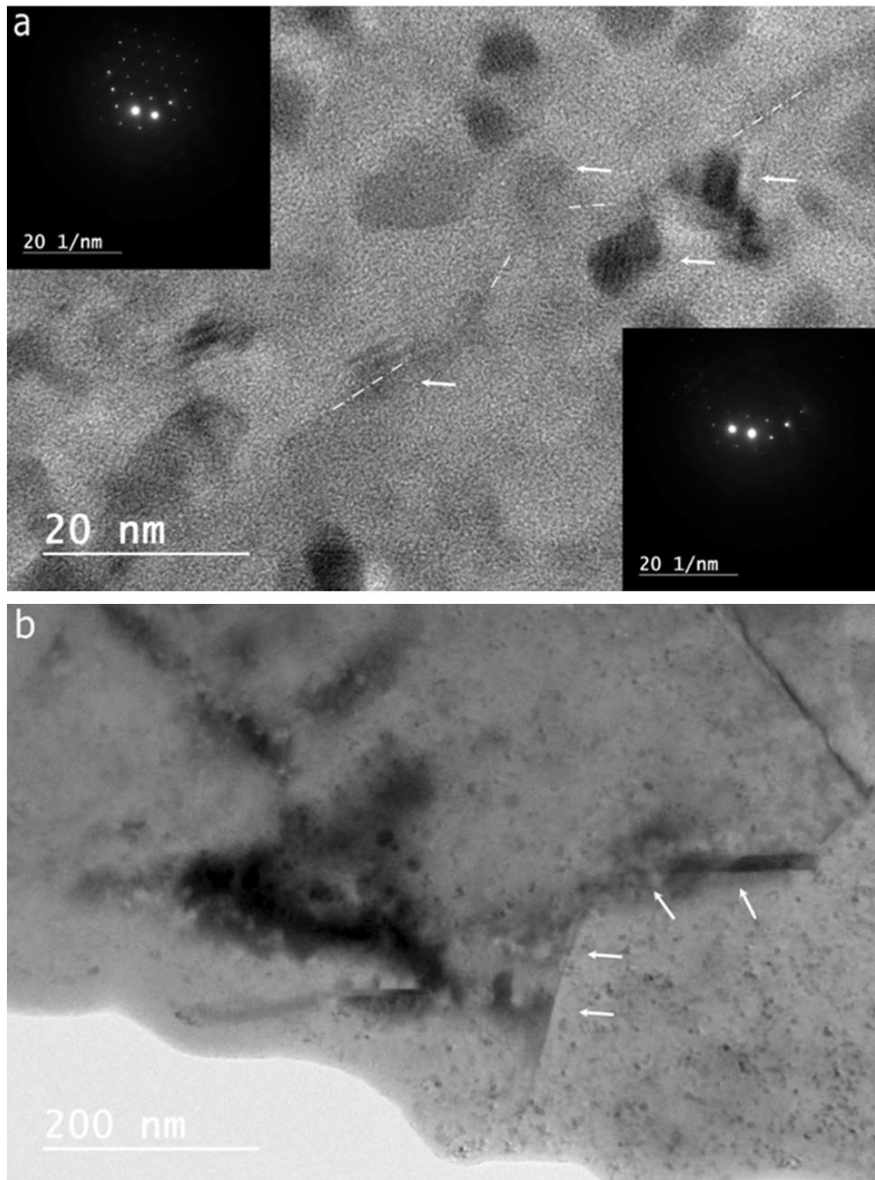


Figure 7: Bright-field transmission electron microscopy images of alloy A extruded at 450 °C with 10 mm/min ram speed showing: (a) a low-angle grain boundary with a local protrusion in the midst of several particles, and (b) a beta precipitate that induces the formation of a grain boundary protrusion indicated by white arrows.

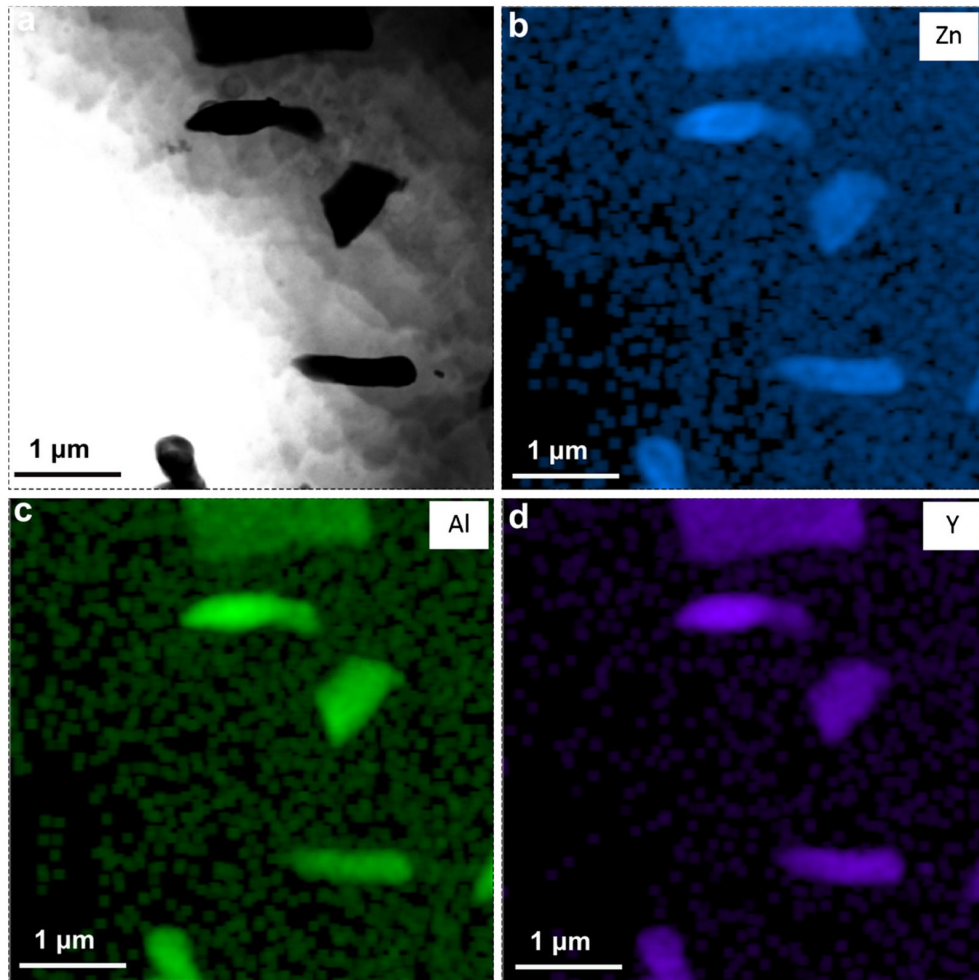


Figure 8: (a) A bright-field transmission electron microscopy image on which energy dispersive X-ray maps of (b) Zn, (c) Al, and (d) Y revealed the abundance of coarse b particles in Alloy A extruded at 450 °C with 10 mm/min ram speed.

RE alloys to precipitate through a four stage process from a super-saturated solid solution [61-63].

3.2.2.4 Nucleation of new orientations In this section, the slow-recrystallizing microstructures are examined to identify early stages of nucleation events between parent grains and their daughters. We carefully examine the misorientation relationships developing before and after the new orientations stabilize, further clarifying the role of GB nucleation.

The image quality map associated with the IPF map in Figure 4(a) reveals that the GB protrusions are consistently accompanied by low-angle boundaries forming at the backside of the crests (Figure 4(a)). Misorientation profiles across these crest areas typically displayed in Figures 4(b) and (c) demonstrate that these low-angle boundaries make misorientation angles evolving between 2 and 10 deg. The gradual formation of these low-angle boundaries at the base of the crests are clearly a trademark of the bulging-induced DDRX grain nucleation mechanism proposed by Sitdikov and Kaibyshev [21]. These authors suggested that the process takes place through three stages. Beginning with SIBM-induced bulging, a subsequent confined strain localization stage promotes formation of a low-angle boundary at the base of the protrusion, which gives rise to an unripe nucleus. Then the process ends up with rotations that stabilize the orientation of the DDRX nucleus as it traps more dislocations at the boundaries. A more detailed schematic based on our observations throughout the extrusion process in this study is shown in Figure 9. It is observed that pancake-shaped grains rotate around either $\langle c \rangle$ -axis or $\langle 10\bar{1}0 \rangle$; which results in formation of fairly wide bands of deformed grains with nearly the same crystallographic orientation (Figures 9(a) and (c)). Afterwards, bulging occurs at the boundaries of deformed bands of grains leading to nucleation of new orientations (Figures 9(d) and (e)).

The IPF maps in Figure 5 captured advanced stages of DDRX grain rotations, leading to different orientations than that of parent grains. These mature orientations are clearly ruled by the axis of rotation which ought to be defined by the type of dislocations generated at the protrusions. Thus, the driving force during the final GB misorientation transformation is granted by the type and density of dislocations being captured by the protruded boundary segments. These dislocations upset the atomic structure of the nucleus GBs, which induces the lattice to rotate to lower the energy state and minimize the density of misfit and interfacial disconnections [64]. Phenomenologically, the total rotation of a fresh nucleus can be approximated to be a function of the density of dislocations trapped in the boundaries surrounding the nucleus. Indeed, the net rotation axis/angle between the DRX grain and nucleus could be interpreted as a total combination of GNDs acting around the nucleus. The net Taylor/rotation axis of active dislocations (or

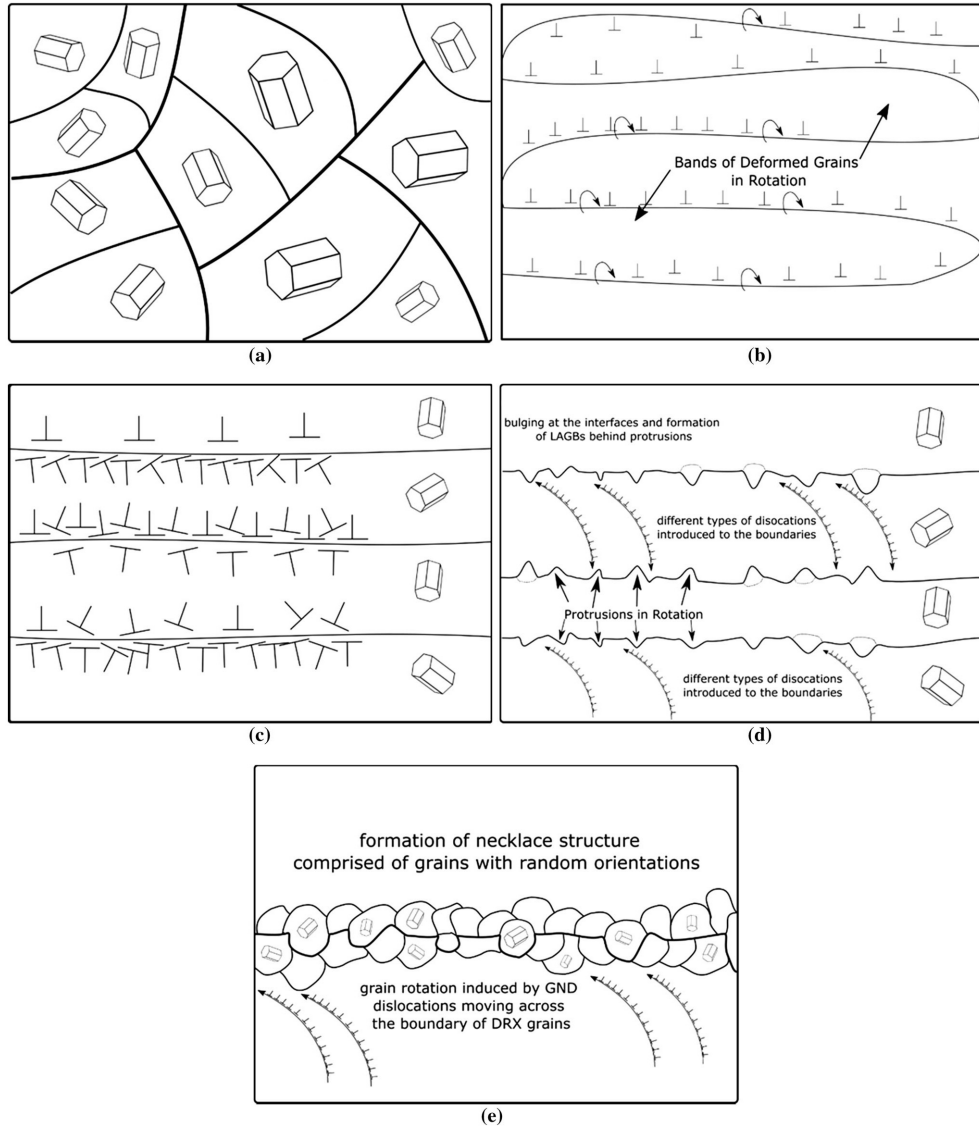


Figure 9: Schematic representation of dynamic recrystallization (DRX) stages, (a) a microstructure with a random texture prior to extrusion, (b) early stages of extrusion expressing immature bands of deformed grains going through rotations induced by continuous dynamic recrystallization (CDRX), (c) formation of stable interfaces between bands of deformed grains after the completion of CDRX, (d) initiation of bulging and formation of low-angle grain boundaries (LAGBs) behind the protrusion that rotate due to intake of variety of geometrically necessary dislocations, (e) formation of necklace structure comprised of DRX grains with random orientations.

slip systems) and the net amount of rotation can be hypothesized to be an arithmetic summation of all active slip systems [15,65].

$$T_{net}^{\vec{}} = \sum_i \gamma_i \vec{T}_i \quad (1)$$

where γ_i is the shear strain induced by i th slip system, and $T_{net}^{\vec{}}$ is a vector in the direction of the rotation axis and with a magnitude equal to the total amount of rotation. DDRX grains with new and stable orientations (i.e., final stage in Figure 9, and RE grains in Figure 5) were observed on interfaces of deformed pancake-shaped grain.

For the case of RE-texture formation from a $\langle 10\bar{1}0 \rangle$ fiber, one can hypothesize a simple two-stage rotation: 28 deg around $[0001]$ direction, demonstrated by Barrett et al. [52] to correspond to the $\langle 13\bar{4}0 \rangle$ twin followed by 28.6 deg around $\langle 10\bar{1}0 \rangle$. This rotation is illustrated in Figure 10(d) for the grain nuclei exhibited in the IPF maps of Figures 10(a) through (c).

The decomposition of the RE-texture rotation into two-step rotation is strongly supported by almost all the texture plots in Figure 1. In fact, the orientations quit the $\langle 10\bar{1}0 \rangle \parallel$ ED parent fiber by edging toward $\langle 11\bar{2}0 \rangle$ fiber and then edge again toward the RE texture. There is actually no orientations directly lying in between the $\langle 10\bar{1}0 \rangle \parallel$ ED and RE-texture component. Texture plots and analyses of the progressive rotations indicate that the rotations proceed in two steps: (1) rotation around $[0001]$ axis, and (2) rotations around $\langle 10\bar{1}0 \rangle$ leading to the final RE texture. According to recent work by some of the authors,[52] rotations around $[0001]$ can create symmetric $\langle \bar{4}310 \rangle$ (28 deg) twins, so further work shall be performed if the remaining rotation around $\langle 10\bar{1}0 \rangle$ is achieved by any $\langle 10\bar{1}0 \rangle$ symmetric tilt twins, and whether there is a transmutation event associated with disconnections. Although pyramidal $\langle a \rangle$ slip alone cannot explain the rotations from the predominant $\langle 10\bar{1}0 \rangle$ orientation to the RE orientation, it could act in concert with basal $\langle a \rangle$ and prismatic $\langle a \rangle$ slip (or even $\langle c+a \rangle$ slip) to bring the local orientation to that of the RE orientation.

The two consecutive rotations would yield a net Taylor axis, which can be approximated by, $[7\bar{2}\bar{5}8]$ and a net rotation angle of ~ 40 deg. Several misorientation axis/angle between parent and DRX grains in the IPF maps were observed to be close to the calculated values. Two instances are represented in the inset IPF of Figure 5(b). Such a high-index Taylor axis is not close to any of the axes known for slip/twinning systems in Mg, and could only be a net sum of multiple rotations that are correlated with the active dislocation modes and how they proceed to relax the boundaries of the ripening nucleus [15]. We conducted a small step size (i.e., $0.2 \mu\text{m}$) EBSD analysis to observe the concurrent activity of dislocations (Figure 11). Figure 11(a) shows the misorientations associated with the activity of

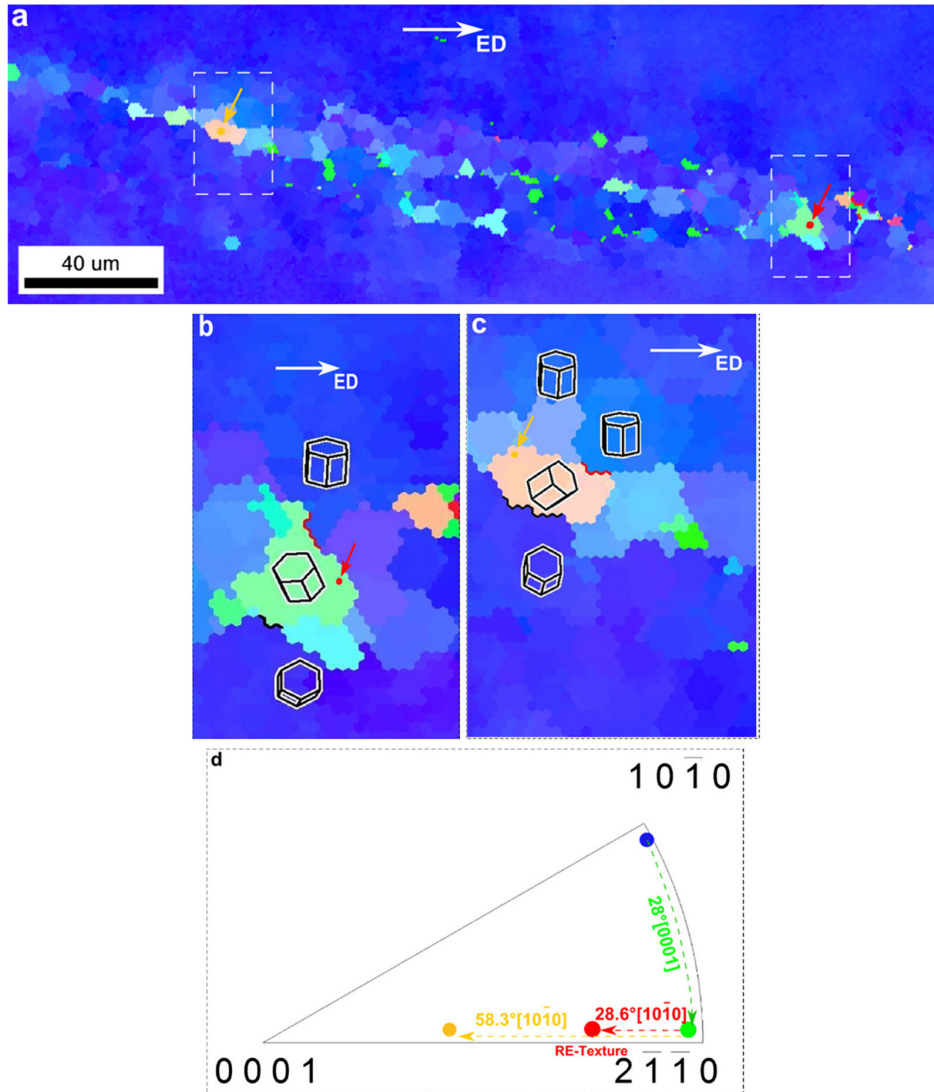


Figure 10: EBSD analyses showing ED-mapped inverse pole figures revealing (a to c) the development of orientation during recrystallization along a high angle grain boundary by the bulging mechanism in alloy A extruded at 450 °C with 10 mm/min ram speed. The rotation could be decomposed into two successive rotations as illustrated in the inverse pole figure of (d). The first rotation corresponds to a 28 deg around [0001] characteristic of {4310} twinning, which is followed by a rotation around $\{<10\bar{1}0>\}$ of various degrees characteristic of basal and $\langle c+a \rangle$ dislocations Taylor axis. The formation of RE texture corresponds to a rotation of around 28.6 deg.

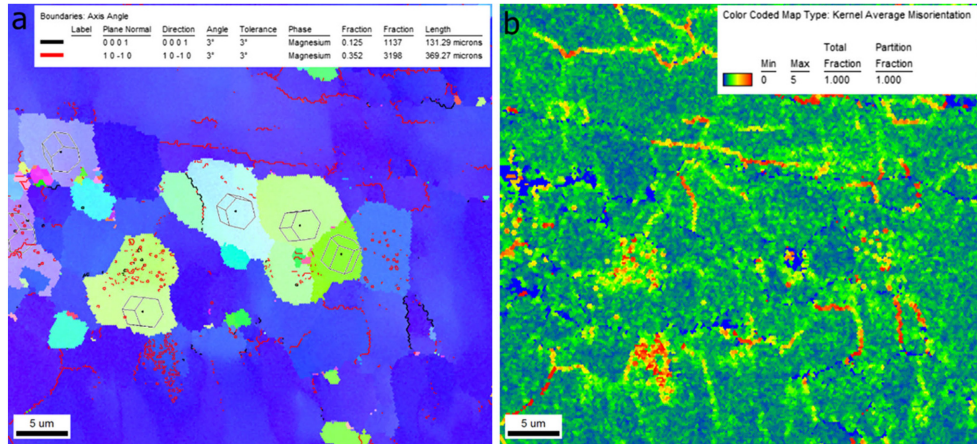


Figure 11: (a) Inverse pole figure ED map of Alloy A extruded at 450 °C with ram speed of 10 mm/min, depicting the presence of misorientations associated with the activity of basal/ $\langle c+a \rangle$ (red lines) and prismatic (black lines) dislocations activity, (b) the corresponding kernel average misorientation (KAM) image indicating the higher degrees of misorientations in the sites of dislocation activity (Color figure online).

basal/ $\langle c+a \rangle$ and prismatic dislocations within and around the fresh DRX grains, and their net induced rotation tallies the deviation from parent orientation. The kernel average misorientation (KAM) map in Figure 11(b) proves that dislocation activation sites commensurate with higher degrees of misorientations, which induce rotations through relaxation into the boundaries.

However, if disconnections were active in the process of GB formation, which is very likely to occur, their shear needs to be taken into account. For instance, if the first rotation is effected by $\{13\bar{4}0\}$ twinning due to relaxation of prismatic dislocation arrays as identified by Barrett et al.,[52] any dislocation that persists, in now the twin lattice, must be transmuted according to the twin shear [53,66-70]. A first inspection based on the correspondence matrix rule[71] yields a transmutation of the basal and pyramidal Taylor axes $\langle d \rangle$, to either $\langle a \rangle$, $(\langle a \rangle + \langle d \rangle)/2$, or $\langle d \rangle + \langle a \rangle/2$, which, strikingly, yield to the RE texture observed in the IPF plots. It should be noted that several combinations of rotations may yield such a net rotation, and the one discussed here is an ideal one. Hence, this mechanism is not further developed in this paper.

In general, the spread around the RE-texture fiber could be attributed to the starting orientation positions of the parent grains within the $\langle 10\bar{1}0 \rangle$ fiber. The inset in Figure 5(b) illustrates the initial and final positions of two parent grains and their respective DRX grains in the IPF (indicated by RE-texture arrows in Figure 5(b)). While both parent grains lie within the RE-texture fiber, the difference re-

main unclear. However, based on the aforementioned Taylor analyses, it is very plausible that all of basal, prismatic, and pyramidal dislocations contribute at the same time to the rotation of the nucleus lattice, only for the amount of absorbed dislocations by the GBs to tally the difference.

It is important to realize that our EBSD inspections in the slowly recrystallized alloys suggest that the contour of RE-texture intensities, measured by XRD, are not dictated by the number fraction of corresponding grain orientations. There is in fact a very significant number of grains with orientations substantially deviated from that fiber, but they remain rather small (Figure 5(b)). Grains closely approaching the center of the RE-texture contours are usually bigger in size. In general, the size of DRX grains scales inversely with the distance from that fiber center. We examine this tendency further in samples extruded with higher speeds. In general, RE texture occurs between $\langle 11\bar{2}1 \rangle \parallel$ ED and $\langle 11\bar{2}1 \rangle \parallel$ ED texture components, which is consistent with published literature [24]. Away from the RE-texture components, the IPF maps in Figure 10 highlight some of the DRX grains with orientations falling close to the $\langle 11\bar{2}3 \rangle \parallel$ ED texture component identified by XRD-measured IPFs of Alloys A and B (Figure 1). This texture would simply arise from a more significant rotation around $\langle 10\bar{1}0 \rangle$ in the aforementioned two-stage rotation, suggesting higher local activity of basal/ $\langle c+a \rangle$ dislocations in some grains [72]. In most cases, these grains correspond to a rotation angle of approximately ~ 58 deg around $\langle 10\bar{1}0 \rangle$.

To summarize the effect of RE additions on the nucleation stage, it is conceived based the experimental observations that nucleation becomes more diverse as a result of higher activity of non-basal slip modes and their recovery during DRX accompanied by high mobility of some special boundaries,[52] though the net rotation is dependent upon the deformation condition and chemical composition [54].

3.2.2.5 Shear banding-induced DRX Shear bands oblique to the ED were captured in Alloy C and reported in the IPF maps of Figure 12. We were not able to capture them prior to the development of DRX grains, which is because of the relatively faster DRX kinetics in this alloy. Gradual rotations across the shear band borders around [0001] axis were omnipresent, and thus indicate that these shear bands were responsible for all recrystallization events that consumed them. Similar to previous observation, there are significant rotations observed inside the shear bands [73]. Few of the extruded billets showed noticeable traces of shear banding, and most DRX occurred within the GB protrusions.

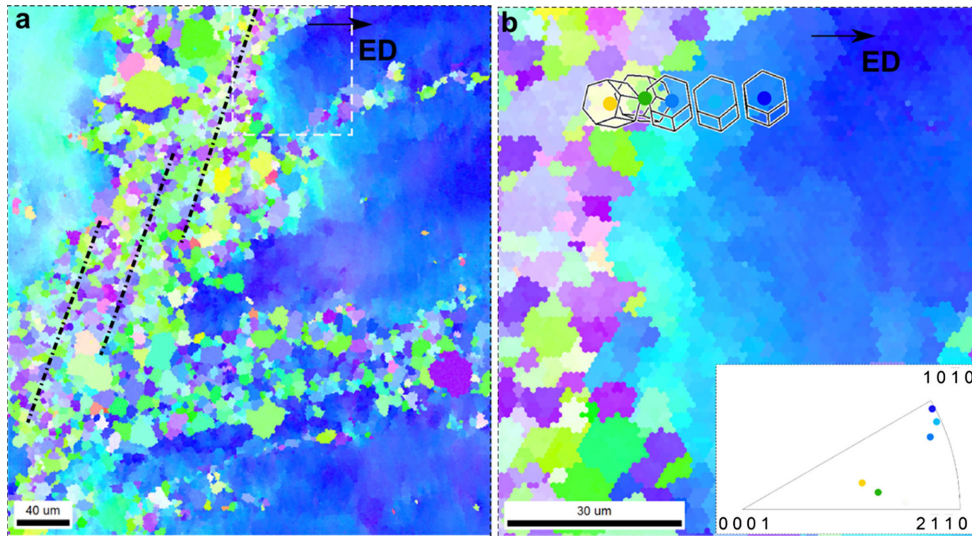


Figure 12: Electron backscattered diffraction analyses showing inverse pole figure ED maps of a region in Alloy C extruded at 450 °C under 10 mm/min ram speed, undergoing (a) continuous dynamic recrystallization at the vicinity of the shear bands and (b) leading to orientations falling close to the RE texture.

4 Static Annealing

The objective of post-deformation annealing was to examine if there is any competition between different orientations during nuclei/grain growth that would lead to a certain growth preference affecting the final texture. Additionally, static annealing provides the partially recrystallized extrudates with sufficient diffusion time for texture modification potential to be assessed. The heat treatments began with isothermal soaking at 450 °C for either 20 or 180 minutes, and ended by water quenching. After 20 minutes of annealing, no discernable nuclei growth was noticed in the slowly recrystallizing Alloys A and B. However, rapidly recrystallizing Alloys C and D began nuclei growth stages while the nucleation stage was not saturated, and their microstructure was still partially recrystallized (Figure 13). IPF plots of three different major grain size ranges reveal similar, weak textures for all detectable ranges, indicating that no growth preferences occur during early stages of static recrystallization (Figure 13).

After 180 minutes of annealing at 450 °C, grain growth is expected to occur with differences in grain growth behavior. It reveals that alloys could not all preserve/grow the nucleated RE grains during static recrystallization (Figure 14). The presented EBSD data in Figure 14 are selected from a series of EBSD scans (5 to 10 scans per sample), and they best represent the texture evolutions through-

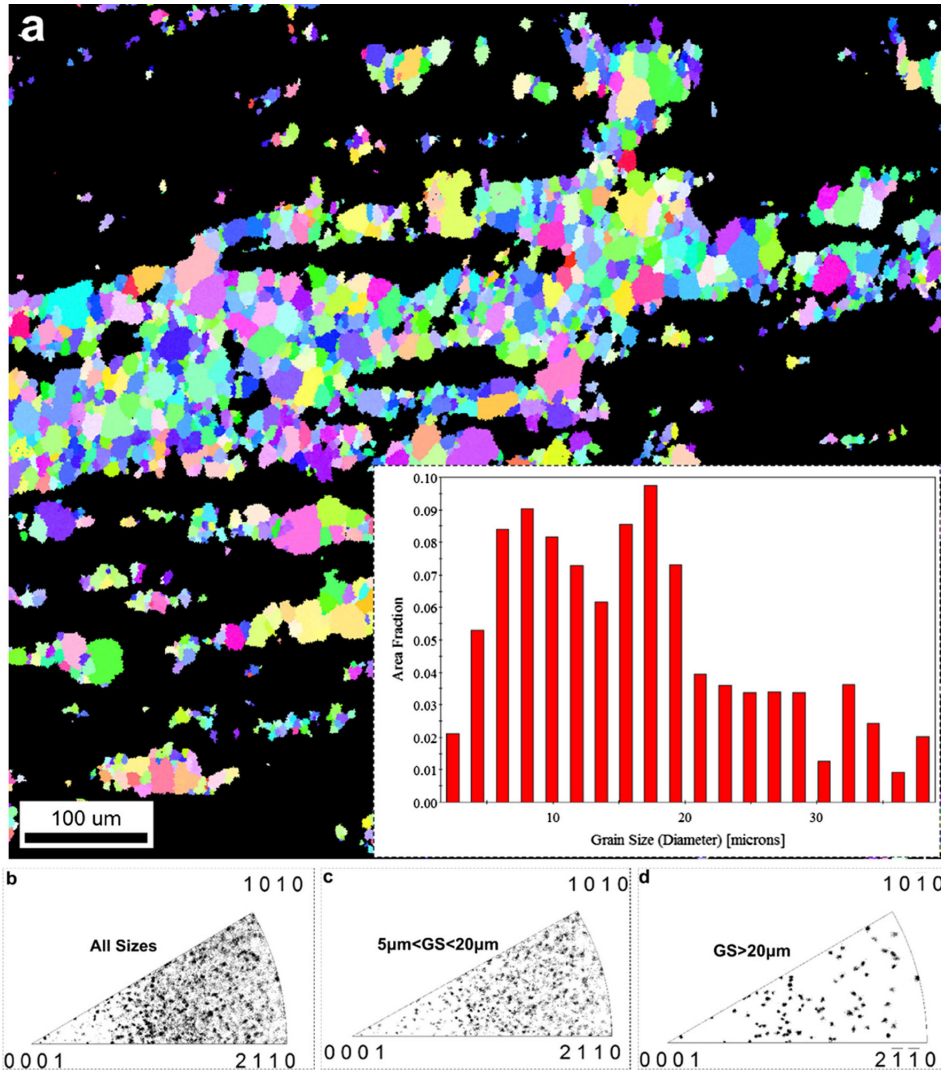


Figure 13: Electron backscattered diffraction with (a) inverse pole figure ED map and grain size distribution of the recrystallized portion of the microstructure of Alloy D extruded at 450 °C with ram speed of 10 mm/min, and post annealed at 450 °C for 20 min. Grain sizes have been partitioned into three ranges and their respective textures are plotted in the inverse pole figures of (b to d).

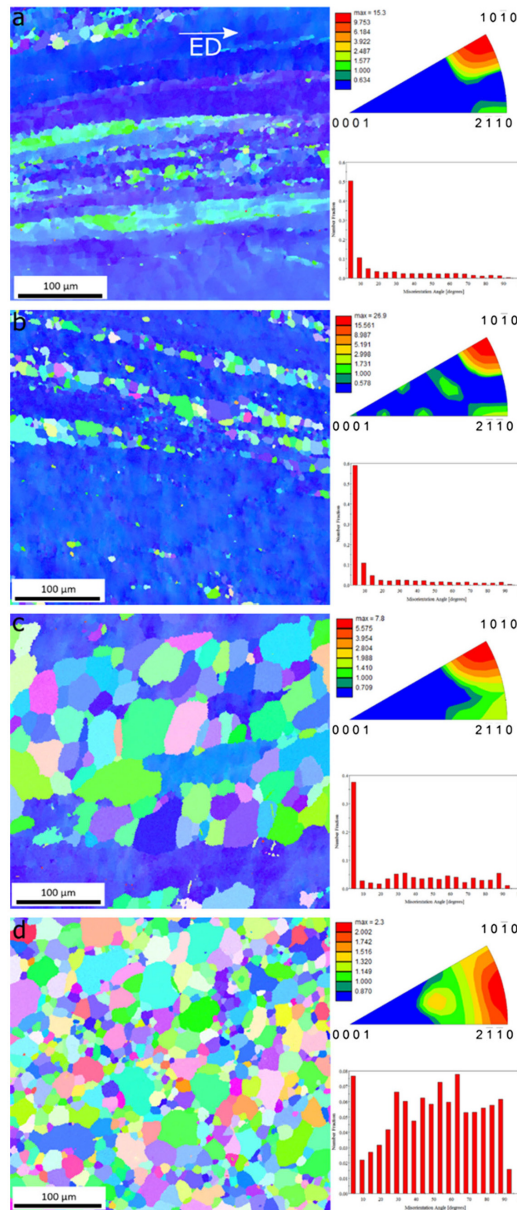


Figure 14: Electron backscattered diffraction analyses showing inverse pole figure ED maps and their corresponding misorientation angle distribution and IPFs, taken from typical regions of (a) Alloy A, (b) Alloy B, (c) Alloy C, and (d) Alloy D after at 450 °C – 10 mm/min extrusion and 450 °C – 3 h annealing.

out the samples. Alloy A with higher content of Zn and no MM strengthen the $\langle 10\bar{1}0 \rangle$ fiber with negligible amount of RE-oriented grains after annealing. The RE-textured grains ended up vanishing, as the amounts of MM was too low to sufficiently bring down the energy contrast level between GBs. Hence, they disappeared during nuclei/grain growth although they were present in the dynamically recrystallized microstructure resulting from high extrusion velocities (Figure 14(a)).

It is worth noting that slow recrystallization kinetics of Alloy A and B suppressed static recrystallization at a temperature as high as 450 °C. Figure 14(b) shows that Alloy B with MM was able to retain only small number of the RE-oriented grains, though it displayed stronger fiber texture. The high portion of GBs with misorientation angles less than 5 deg is due to the formation of sub-grains during static recrystallization, as these alloys failed to express static grain growth (Figure 14(b)). Moreover, we tried eliminating misorientation values smaller than 10 deg to better observe the misorientation distribution of high angle boundaries. However, the misorientation profiles appeared to express nearly the same distribution.

Alloy C, with high nucleation rate and a strong RE texture after extrusion, showed substantial nuclei growth, but the RE-textured grains nearly completely vanished after static recrystallization (Figure 14(c)). The only composition that fully met the requirements of fast nucleation rates and optimum Zn, Y, and REE additions for isotropic grain growth was Alloy D, and therefore, it developed a fairly weak texture (max ntensity of 2.3 m.r.d.) after annealing (Figure 14(d)). This is a proof that MM additions promote RE-texture persistence. The broader distribution of misorientation angles in Alloy D after static recrystallization could be ascribed to a more isotropic grain growth process, which may be explained by a GB co-segregation effect that decreases the anisotropy in GB energy and mobility (Figure 6). The homogeneous spectrum of misorientation angles indicate that the lower Zn and high MM contents allowed all type of GBs to compete favorably with each other even during growth despite its high kinetics. Al-Samman and Li [41] observed that their MM-containing alloy developed the most uniform misorientation distribution. Their results agree well with the more uniform misorientation distribution shown by Alloy D in the near fully recrystallized state in Figure 14(d). Here, we propose that isotropic grain growth is essential for the survival of new orientations nucleated during dynamic/static recrystallization, which intensifies texture components deviated from $\langle 10\bar{1}0 \rangle$ ED with higher intensities around RE texture and renders them identifiable. The detailed explication for the higher intensities around RE-texture component is described in another work by some of the present authors [54].

A stark comparison between the texture of high-speed extrusion and low-speed extrusion followed by annealing, particularly for Alloy D, reveals the key influ-

ence of grain growth on texture modification (compare Figures 1 and 14) [74]. Either dynamic or static nuclei/grain growth, in the presence of optimum RE and Zn addition, favor texture weakening in similar manners. In fact, regardless of the type of growth, it is the driving force for growth of nuclei or grains that is essential. For instance, slowly extruded Alloy D with strong fiber texture (Figure 1(d)) displayed the weakest texture intensity after it was fully recrystallized (Figure 14(d)). Additionally, high-speed extrusion yielded more driving force for dynamic nuclei growth, which resulted in significant texture weakening as well (Figure 14(d)). Therefore, this observation substantiates the fact that texture modification through RE addition would not be effective unless the driving force for growth is supplied. In other words, homogeneous growth seems to be essential, in terms of texture modification, for the effectiveness of RE-driven randomly nucleated grains.

Hence, when designing RE-containing Mg alloys, one must predict final texture of the product based on the mutual interaction of all alloying elements, Zn and RE in particular. REEs are needed for triggering new texture components, but if accompanied by relatively higher amount of Zn and Y, they can also slow down the kinetics of DRX through co-segregation to GBs,[49] thus sharpening the texture by preserving the deformed parent grains in the microstructure (e.g., Alloy B). Moreover, one may thoroughly optimize processing variables (e.g., extrusion temperature, speed and area reduction ratio) to obtain the desired texture upon processing.

5 Conclusions

This paper has helped clarify the mechanisms responsible for the origin of the “RE-texture” in RE-containing magnesium alloys.

1. The RE-texture components correspond to orientations lying between $\langle 11\bar{2}1 \rangle$ ED and $\langle 11\bar{2}1 \rangle \parallel$ ED with a marked concentration close to $\langle 22\bar{4}3 \rangle \parallel$ ED.
2. The main nucleation sites of grains with these characteristic orientations of the RE texture correspond to GB protrusions along GBs between bands of deformed grains. GB bulging is shown to be the predominant RE-texture nucleation mechanism. This mechanism is consistent with the widely reported mechanism of DDRX. TEM in this work revealed particles at GBs close to protrusions, which is reminiscent of particle pinning, and promotes SIBM.
3. EBSD of the new orientations that form within the protrusions show that they correspond to contributions from $\langle 10\bar{1}0 \rangle$ and $[0001]$ rotation axes in

the same protruded region. This is consistent with a concomitant action of multiple slip modes.

4. Continuous DRX contributed to the formation and rotation of sub-grains inside the bands of deformed grains, which resulted in the thickening of the bands and texture sharpening.
5. While shear localization events were found to occur in these alloys, they were far from having a dominant effect on the overall texture, and in all relevant cases, bulging-induced DDRX remains the prevailing mechanism for texture modification.
6. After static recrystallization and nuclei/grain growth, even more random textures are attained. According to recent work,[75] this phenomenon is consistent with REE segregation to GBs, which could alter the effective GB energy and mobility variations among GB types. Future work should focus on further illuminating this important aspect of RE addition on the final texture in Mg alloys.

Acknowledgements

All the experiments for this research was conducted in Center for Advanced Vehicular Systems (CAVS) at Mississippi State University. The authors would like to thank Dr. Sean R. Agnew at University of Virginia for intensive and informative discussions on the results of this study. This research was sponsored by the Army Research Laboratory and was accomplished under Cooperative Agreement Number W911NF-15-2-0025. The views and conclusions contained in this document are those of the authors and should not be interpreted as representing the official policies, either expressed or implied, of the Army Research Laboratory or the US Government. The US Government is authorized to reproduce and distribute reprints for Government purposes notwithstanding any copyright notation herein.

References

1. A. Imandoust, C. Barrett, T. Al-Samman, K. Inal, and H. El Kadiri: *J. Mater. Sci.*, 2017, vol. 52, pp. 1–29.
2. S.R. Agnew, P. Mehrotra, T.M. Lillo, G.M. Stoica, and P.K. Liaw: *Acta Mater.*, 2005, vol. 53, pp. 3135–46.

3. S.R. Agnew and Ö . Duygulu: *Int. J. Plast.*, 2005, vol. 21, pp. 1161–93.
4. S.R. Agnew, J.A. Horton, T.M. Lillo, and D.W. Brown: *Scripta Mater.*, 2004, vol. 50, pp. 377–81.
5. S.R. Agnew, C.N. Tomé , D.W. Brown, T.M. Holden, and S.C. Vogel: *Scripta Mater.*, 2003, vol. 48, pp. 1003–08.
6. M. Barnett, M. Nave, and C. Bettles: *Mater. Sci. Eng. A*, 2004, vol. 386, pp. 205–11.
7. J. Bohlen, S.B. Yi, J. Swiostek, D. Letzig, H.G. Brokmeier, and K.U. Kainer: *Scripta Mater.*, 2005, vol. 53, pp. 259–64.
8. J.A. del Valle, F. Carreño, and O.A. Ruano: *Acta Mater.*, 2006, vol. 54, pp. 4247–59.
9. B. Mordike and T. Ebert: *Mater. Sci. Eng. A*, 2001, vol. 302, pp. 37–45.
10. H. Watanabe, T. Mukai, and K. Ishikawa: *J. Mater. Process. Technol.*, 2007, vol. 182, pp. 644–47.
11. S. Agnew, M. Yoo, and C. Tome: *Acta Mater.*, 2001, vol. 49, pp. 4277–89.
12. I. Ulacia, N.V. Dudamell, F. Gálvez, S. Yi, M.T. Pérez-Prado, and I. Hurtado: *Acta Mater.*, 2010, vol. 58, pp. 2988–98.
13. L.L. Chang, E.F. Shang, Y.N. Wang, X. Zhao, and M. Qi: *Mater. Charact.*, 2009, vol. 60, pp. 487–91.
14. Y. Chino, K. Kimura, and M. Mabuchi: *Mater. Sci. Eng. A*, 2008, vol. 486, pp. 481–88.
15. J.P. Hadorn, K. Hantzsche, S. Yi, J. Bohlen, D. Letzig, and S.R. Agnew: *Metall. Mater. Trans. A*, 2012, vol. 43A, pp. 1363–75.
16. T. Al-Samman and G. Gottstein: *Mater. Sci. Eng. A*, 2008, vol. 490, pp. 411–20.
17. M.R. Barnett: *Mater. Trans.*, 2003, vol. 44, pp. 571–77.
18. J. Del Valle and O.A. Ruano: *Mater. Sci. Eng. A*, 2008, vol. 487, pp. 473–80.
19. S.M. Fatemi-Varzaneh, A. Zarei-Hanzaki, and H. Beladi: *Mater. Sci. Eng. A*, 2007, vol. 456, pp. 52–57.
20. A. Galiyev, R. Kaibyshev, and G. Gottstein: *Acta Mater.*, 2001, vol. 49, pp. 1199–1207.
21. O. Sitdikov and R. Kaibyshev: *Mater. Trans.*, 2001, vol. 42, pp. 1928–37.

22. P. Changizian, A. Zarei-Hanzaki, M. Ghambari, and A. Imandoust: *Mater. Sci. Eng. A*, 2013, vol. 582, pp. 8–14.
23. J. Bohlen, S. Yi, D. Letzig, and K.U. Kainer: *Mater. Sci. Eng. A*, 2010, vol. 527, pp. 7092–98.
24. N. Stanford: *Mater. Sci. Eng. A*, 2010, vol. 527, pp. 2669–77.
25. N. Stanford and M.R. Barnett: *Mater. Sci. Eng. A*, 2008, vol. 496, pp. 399–408.
26. S. Sandlöbes, M. Friák, S. Zaeferrer, A. Dick, S. Yi, D. Letzig, Z. Pei, L.F. Zhu, J. Neugebauer, and D. Raabe: *Acta Mater.*, 2012, vol. 60, pp. 3011–21.
27. S. Sandlöbes, S. Zaeferrer, I. Schestakow, S. Yi, and R. Gonzalez-Martinez: *Acta Mater.*, 2011, vol. 59, pp. 429–39.
28. S. Agnew, R. Mulay, F. Polesak, C. Calhoun, J. Bhattacharyya, and B. Clausen: *Acta Mater.*, 2013, vol. 61, pp. 3769–80.
29. K. Máthis, G. Csiszár, J. Čapek, J. Gubicza, B. Clausen, P. Lukáš , A. Vinogradov, and S. Agnew: *Int. J. Plast.*, 2015, vol. 72, pp. 127–50.
30. J.P. Hadorn, R.P. Mulay, K. Hantzsche, S. Yi, J. Bohlen, D. Letzig, and S.R. Agnew: *Metall. Mater. Trans. A*, 2012, vol. 44A, pp. 1566–76.
31. R.K. Mishra, A.K. Gupta, P.R. Rao, A.K. Sachdev, A.M. Kumar, and A.A. Luo: *Scripta Mater.*, 2008, vol. 59, pp. 562–65.
32. Y. Chino, M. Kado, and M. Mabuchi: *Mater. Sci. Eng. A*, 2008, vol. 494, pp. 343–49.
33. K. Hantzsche, J. Bohlen, J. Wendt, K.U. Kainer, S.B. Yi, and D. Letzig: *Scripta Mater.*, 2010, vol. 63, pp. 725–30.
34. N. Stanford, D. Atwell, A. Beer, C. Davies, and M.R. Barnett: *Scripta Mater.*, 2008, vol. 59, pp. 772–75.
35. M. Barnett, A. Sullivan, N. Stanford, N. Ross, and A. Beer: *Scripta Mater.*, 2010, vol. 63, pp. 721–24.
36. R. Cottam, J. Robson, G. Lorimer, and B. Davis: *Mater. Sci. Eng. A*, 2008, vol. 485, pp. 375–82.
37. N. Stanford: *Mater. Sci. Eng. A*, 2013, vol. 565, pp. 469–75.
38. N. Stanford, M. Callaghan, and B. De Jong: *Mater. Sci. Eng. A*, 2013, vol. 565, pp. 459–68.

39. E. Ball and P. Prangnell: *Scripta Metall. Mater.*, 1994, vol. 31, pp. 111–16.
40. L. Mackenzie, B. Davis, F. Humphreys, and G. Lorimer: *Mater. Sci. Technol.*, 2007, vol. 23, pp. 1173–80.
41. T. Al-Samman and X. Li: *Mater. Sci. Eng. A*, 2011, vol. 528, pp. 3809–22.
42. J. Robson, D. Henry, and B. Davis: *Acta Mater.*, 2009, vol. 57, pp. 2739–47.
43. J.P. Hadorn, K. Hantzsche, S. Yi, J. Bohlen, D. Letzig, J.A. Wollmershauser, and S.R. Agnew: *Metall. Mater. Trans. A*, 2011, vol. 43A, pp. 1347–62.
44. J. Hadorn, T. Sasaki, T. Nakata, T. Ohkubo, S. Kamado, and K. Hono: *Scripta Mater.*, 2014, vol. 93, pp. 28–31.
45. J.F. Nie, K. Oh-ishi, X. Gao, and K. Hono: *Acta Mater.*, 2008, vol. 56, pp. 6061–76.
46. J. Nie, Y. Zhu, J. Liu, and X.-Y. Fang: *Science*, 2013, vol. 340, pp. 957–60.
47. L. Mackenzie and M. Pekguleryuz: *Scripta Mater.*, 2008, vol. 59, pp. 665–68.
48. M. Steiner, J. Bhattacharyya, and S. Agnew: *Acta Mater.*, 2015, vol. 95, pp. 443–55.
49. Z.R. Zeng, Y.M. Zhu, S.W. Xu, M.Z. Bian, C.H.J. Davies N. Birbilis, and J.F. Nie: *Acta Mater.*, 2016, vol. 105, pp. 479–94.
50. G. Song: *Adv. Eng. Mater.*, 2005, vol. 7, pp. 563–86.
51. R. Hielscher and H. Schaeben: *J. Appl. Crystallogr.*, 2008, vol. 41, pp. 1024–37.
52. C.D. Barrett, A. Imandoust, A.L. Oppedal, K. Inal, M.A. Tschopp, and H. El Kadiri: *Acta Mater.*, 2017, vol. 128, pp. 270–83.
53. C.D. Barrett and H. El Kadiri: *Acta Mater.*, 2014, vol. 63, pp. 1–15.
54. A. Imandoust, C.D. Barrett, A.L. Oppedal, W.R. Whittington Y. Paudel, and H. El Kadiri: *Acta Mater.*, 2017, vol. 138, pp. 27–41.
55. A. Rollett, F. Humphreys, G.S. Rohrer, and M. Hatherly: *Recrystallization and Related Annealing Phenomena*, Elsevier, Amsterdam, 2004.
56. J. Wang and I.J. Beyerlein: *Metall. Mater. Trans. A*, 2012, vol. 43A, pp. 3556–69.
57. G. Bruggeman, G. Bishop, and W. Hartt: *The Nature and Behavior of Grain Boundaries*, Springer, New York, 1972, pp. 83–122.

58. Z.R. Zeng, M.Z. Bian, S.W. Xu, C.H.J. Davies, N. Birbilis, and J.F. Nie: *Scripta Mater.*, 2015, vol. 108, pp. 6–10.
59. G.B. Stephenson: *Acta Metall.*, 1988, vol. 36, pp. 2663–83.
60. A. Inoue, Y. Kawamura, M. Matsushita, K. Hayashi, and J. Koike: *J. Mater. Res.*, 2001, vol. 16, pp. 1894–1900.
61. L. Li: *Mater. Sci. Eng. A*, 2011, vol. 528, pp. 7178–85.
62. L. Li: *J. Alloys Compd.*, 2013, vol. 555, pp. 255–62.
63. S.M. He, X.Q. Zeng, L.M. Peng, X. Gao, and J.F. Nie: *J. Alloys Compd.*, 2006, vol. 421, pp. 309–13.
64. J.P. Hirth, R.C. Pond, and J. Lothe: *Acta Mater.*, 2006, vol. 54, pp. 4237–45.
65. Y.B. Chun, M. Battaini, C.H.J. Davies, and S.K. Hwang: *Metall. Mater. Trans. A*, 2010, vol. 41A, pp. 3473–87.
66. C. Barrett, H. El Kadiri, and M. Tschopp: *J. Mech. Phys. Solids*, 2012, vol. 60, pp. 2084–99.
67. H. El Kadiri, C.D. Barrett, J. Wang, and C.N. Tomé : *Acta Mater.*, 2015, vol. 85, pp. 354–61.
68. H. El Kadiri, J. Kapil, A. Oppedal, L. Hector, S.R. Agnew M. Cherkaoui, and S. Vogel: *Acta Mater.*, 2013, vol. 61, pp. 3549–63.
69. J. Jordon, H. Brown, H. El Kadiri, H. Kistler, R. Lett, J. Baird, and A. Luo: *Int. J. Fatigue*, 2013, vol. 51, pp. 8–14.
70. A. Oppedal, H. El Kadiri, C. Tome´ , S.C. Vogel, and M. Horstemeyer: *Philos. Mag.*, 2013, vol. 93, pp. 4311–30.
71. M. Niewczas: *Acta Mater.*, 2010, vol. 58, pp. 5848–57.
72. L. Toth, P. Gilormini, and J. Jonas: *Acta Metall.*, 1988, vol. 36, pp. 3077–91.
73. I. Basu, T. Al-Samman, and G. Gottstein: *Mater. Sci. Eng. A*, 2013, vol. 579, pp. 50–56.
74. J.W. Senn and S.R. Agnew: *Proc. Magnes. Technol.*, 2008, vol. 2008, pp. 153–58.
75. C.D. Barrett, A. Imandoust, and H. El Kadiri: *Scripta Mater.*, 2018, vol. 146, pp. 46–50.